The Astrophysical Journal, 931:104 (16pp), 2022 June 1 https://doi.org/10.3847/1538-4357/ac69da

Three-dimensional General-relativistic Simulations of Neutrino-driven Winds from Rotating Proto-neutron Stars

Dhruv Desai[1], Daniel M. Siegel[2,3], and Brian D. Metzger[1,4]
[1] Department of Physics and Columbia Astrophysics Laboratory, Columbia University, Pupin Hall, New York, NY 10027, USA; dkd2117@columbia.edu
[2] Perimeter Institute for Theoretical Physics, Waterloo, Ontario N2L 2Y5, Canada
[3] Department of Physics, University of Guelph, Guelph, Ontario N1G 2W1, Canada
[4] Center for Computational Astrophysics, Flatiron Institute, 162 5th Ave, New York, NY 10010, USA
Received 2022 March 30; revised 2022 April 18; accepted 2022 April 21; published 2022 May 31

Abstract

We explore the effects of rapid rotation on the properties of neutrino-heated winds from proto-neutron stars (PNS) formed in core-collapse supernovae or neutron-star mergers by means of three-dimensional general-relativistic hydrodynamical simulations with M0 neutrino transport. We focus on conditions characteristic of a few seconds into the PNS cooling evolution when the neutrino luminosities obey $L_{\nu_e} + L_{\bar{\nu}_e} \approx 7 \times 10^{51}\,\mathrm{erg\,s^{-1}}$, and over which most of the wind mass loss will occur. After an initial transient phase, all of our models reach approximately steady-state outflow solutions with positive energies and sonic surfaces captured on the computational grid. Our nonrotating and slower rotating models (angular velocity relative to Keplerian $\Omega/\Omega_{\rm K} \lesssim 0.4$; spin period $P \gtrsim 2$ ms) generate approximately spherically symmetric outflows with properties in good agreement with previous PNS wind studies. By contrast, our most rapidly spinning PNS solutions ($\Omega/\Omega_{\rm K} \gtrsim 0.75$; $P \approx 1$ ms) generate outflows focused in the rotational equatorial plane with much higher mass-loss rates (by over an order of magnitude), lower velocities, lower entropy, and lower asymptotic electron fractions, than otherwise similar nonrotating wind solutions. Although such rapidly spinning PNS are likely rare in nature, their atypical nucleosynthetic composition and outsized mass yields could render them important contributors of light neutron-rich nuclei compared to more common slowly rotating PNS birth. Our calculations pave the way to including the combined effects of rotation and a dynamically important large-scale magnetic field on the wind properties within a three-dimensional GRMHD framework.

Unified Astronomy Thesaurus concepts: Stellar winds (1636); Neutron stars (1108); Supernova remnants (1667); R-process (1324); General relativity (641); High energy astrophysics (739)

1. Introduction

The aftermath of a successful core-collapse supernova explosion is the formation of a hot, proto-neutron star (PNS) that cools via the emission of thermal neutrinos over the ensuing seconds, radiating the gravitational binding energy of the star (e.g., Burrows & Lattimer 1986; Pons et al. 1999; Roberts 2012; see Roberts & Reddy 2017 for a recent review). These neutrinos deposit energy into the atmosphere of the PNS, driving an outflow of mass known as the *neutrino-driven wind* (e.g., Duncan et al. 1986; Qian & Woosley 1996; Thompson et al. 2001). A similar PNS cooling phase, and concomitant neutrino-driven wind, accompanies the cooling evolution of the remnant of a neutron star merger (e.g., Dessart et al. 2009; Metzger & Fernández 2014; Perego et al. 2014; Kaplan et al. 2014; Metzger et al. 2018), in cases when the remnant does not promptly collapse into a black hole.

The neutrino wind has long been considered a potential site for the nucleosynthesis of heavy neutron-rich isotopes through the rapid neutron-capture process (*r*-process; e.g., Meyer et al. 1992; Takahashi et al. 1994; Woosley et al. 1994). The many past studies of neutrino-driven winds have primarily been focused on spherically symmetric, nonrotating PNS winds accelerated by thermal pressure (e.g., Kajino et al. 2000; Sumiyoshi et al. 2000; Otsuki et al. 2000; Thompson et al. 2001; Arcones et al. 2007; Fischer et al. 2010; Roberts et al. 2010, 2012; Arcones & Montes 2011; Fischer et al. 2012 ; Martínez-Pinedo et al. 2012). This body of work has led to the conclusion that normal PNS winds fail to achieve the conditions necessary for nucleosynthesis to reach the third *r*-process peak around an atomic mass number $A \sim 195$. The latter requires an outflow with a combination of high specific entropy s_∞, short expansion timescale $\tau_{\rm exp}$, and low electron fraction Y_e (Hoffman et al. 1997; Meyer & Brown 1997) as it passes through the radii where seed nuclei form. In particular, even for only moderately neutron-rich conditions (e.g., $0.4 \lesssim Y_e \lesssim 0.5$) a sufficiently large value of $s_\infty^3/(Y_e^3 \tau_{\rm exp})$ results in a high ratio of neutrons to seed nuclei, and hence a successful heavy *r* process, by trapping protons into α particles as a result of the freeze-out of the neutron-modified triple-α reaction ^{4}He(αn,γ)^{9}Be(α,n)^{12}C (e.g., Meyer et al. 1992; Woosley & Hoffman 1992).

Several ideas have been proposed beyond the standard scenario in order to achieve a high neutron-to-seed ratio, and a successful second- or third-peak *r* process. These include postulating the existence of additional sources of heating (e.g., damping of convectively excited waves; Suzuki & Nagataki 2005; Metzger et al. 2007; Gossan et al. 2020) or by resorting to extreme parameters, such as massive $\gtrsim 2.2\,M_\odot$ neutron stars (Wanajo 2013) or those with extremely strong magnetic fields ("magnetars"; Thompson 2003; Thompson et al. 2004; Metzger et al. 2007, 2008; Vlasov et al. 2014, 2017).

Insofar as rapidly spinning magnetars are contenders for the central engines of gamma-ray bursts (e.g., Thompson et al.

2004; Bucciantini et al. 2007; Metzger et al. 2011b), the nuclear composition of their outflows may have important implications for the gamma-ray emission mechanism (e.g., Beloborodov 2010) and the composition of cosmic rays accelerated in the relativistic jet (e.g., Metzger et al. 2011a; Bhattacharya et al. 2021). Nevertheless, the physical processes responsible for the creation of an ordered large-scale magnetic field during the PNS phase remain uncertain and subject to active research (e.g., Raynaud et al. 2020).

Two of the potentially important ingredients in neutrino-driven winds, which we explore in this work, are the effects of general relativity (GR) and rapid rotation. The deeper gravitational potential well of the PNS present in GR tends to increase the entropy of the outflows relative to an otherwise equivalent model with Newtonian gravity by around 50% (e.g., Cardall & Fuller 1997; Otsuki et al. 2000; Thompson et al. 2001). Rotation, on the other hand, will generally act to decrease the entropy of the outflows, by reducing the effective gravitational potential due to centrifugal effects (e.g., Metzger et al. 2007). Extremely rapid rotation could in principle also reduce the wind electron fraction, in part because fewer neutrino absorptions per nucleon are necessary to unbind the wind material near the rotational equator, allowing the outflow's composition to remain closer to that of the highly neutron-rich PNS surface (e.g., Metzger et al. 2008).

Beyond parametrized one-dimensional models (e.g., Duncan et al. 1986; Qian & Woosley 1996; Thompson et al. 2001), numerical work on neutrino-driven winds has focused on one-dimensional and two-dimensional Newtonian hydrodynamical simulations with approximate neutrino transport (e.g., Arcones et al. 2007; Dessart et al. 2009; Fischer et al. 2010; Hüdepohl et al. 2010; Roberts et al. 2010; Nakazato et al. 2013; Arcones & Janka 2011). Three-dimensional simulations have so far concentrated on the neutron star merger case, including the Newtonian simulations by Perego et al. (2014). Three-dimensional simulations in the context of core-collapse supernovae have so far focused on the early post-bounce evolution and the explosion mechanism itself, rather than on the long-term cooling evolution of the PNS (e.g., Burrows et al. 2020).

In this paper, we explore the effects of rapid rotation on neutrino-heated PNS winds by means of general-relativistic hydrodynamical simulations with approximate neutrino transport. Rather than employing initial conditions for the PNS motivated by self-consistent supernova or merger simulations, we instead follow previous work (Kaplan et al. 2014) in constructing parameterized models for the thermodynamic and compositional structure of the PNS that result in neutrino luminosities and energies consistent with those predicted by successful supernova and neutron star merger simulations to occur a few seconds after the birth of the star (the epoch over which most of the integrated wind mass loss occurs). By first isolating the effects of rapid rotation in the purely hydrodynamical context, our work here also paves the way for future simulations which will include additional effects, such as the presence of a strong ordered magnetic field.

This paper is organized as follows. In Section 2, we describe the physical setup, initial conditions, and numerical code used to perform our neutrino-wind simulations. In Section 3, we describe our results, starting with nonrotating PNS wind solutions and then moving on to the rotating cases. As we shall discuss, rapid (approximately millisecond period) rotation can have large effects on essentially all of the key wind properties. In Section 4, we summarize our conclusions and speculate on the potential role of rapidly spinning PNS birth as sources of heavy neutron-rich nuclei.

2. Methodology

2.1. Numerical Evolution Code

Our simulations of PNS winds are performed in three-dimensional general-relativistic hydrodynamics (GRHD) using a modified version of `GRHydro` (Mösta et al. 2014) as described in Siegel & Metzger (2018), which is built on the open-source `Einstein Toolkit`[5] (Goodale et al. 2003; Schnetter et al. 2004; Thornburg 2004; Löffler et al. 2012; Babiuc-Hamilton et al. 2019). This code implements the equations of ideal general-relativistic magnetohydrodynamics with a finite-volume scheme using piecewise parabolic reconstruction (Colella & Woodward 1984) and the approximate HLLE Riemann solver (Harten et al. 1983). Recovery of primitive variables is implemented using the framework presented in Siegel et al. (2018) and Siegel & Mösta (2018), which provides support for any composition-dependent, three-parameter equation of state (EOS). The magnetic field is evolved using a variant of constrained transport (the "flux-CT" method; Tóth 2000) in order to maintain the solenoidal constraint. In the present study of purely hydrodynamical winds, however, the magnetic field is ignored. Its initial field strength is set to a very small number and monitored throughout the evolution to ensure that it does not impact the dynamics of the simulation.

Although the code is capable of evolving spacetime, the present set of simulations employs a fixed metric for computational efficiency, determined self-consistently from the matter distribution of the initial conditions (Section 2.2). A fixed spacetime is a good approximation here, because the star's structure remains nearly constant in time and less than a fraction of $\sim 10^{-5}$ of the star's mass is removed by winds over the duration of the simulation. We also performed a test simulation including the full metric evolution, which exhibited only small differences from the fixed-metric case.

We consider both nonrotating and rotating PNS models (Section 2.2). The computational domain is set up as a Cartesian grid hierarchy consisting of one base grid and six nested refinement levels for our nonrotating PNS model. In our fiducial nonrotating PNS model nrot−HR, the finest and smallest grid is a $15 \times 15 \times 15$ km box centered at the origin and the center of the star, with a resolution of $\Delta x \simeq 225$ m. The size of the largest box is $960 \times 960 \times 960$ km, which allows us to capture the wind zone and to determine the asymptotic properties of the wind. In comparison, the grid setup for our most rapidly rotating PNS models (`rot.7-MR`, `rot.6-MR`) has one less refinement level, with the finest and smallest grid being a $30 \times 30 \times 30$ km box; this is necessary to resolve the high-velocity outflows from the PNS surface out to larger radii. All of our rotating models employ a spatial resolution on the finest grid of $\Delta x \simeq 450$ m.

We find that our adopted resolution is not sufficient to resolve the neutrino decoupling region near the PNS surface, which we quantify in Figure 1 using the optical depth scale height near the neutrinosphere obtained once our wind solutions have reached a steady state. This would require a

[5] http://einsteintoolkit.org

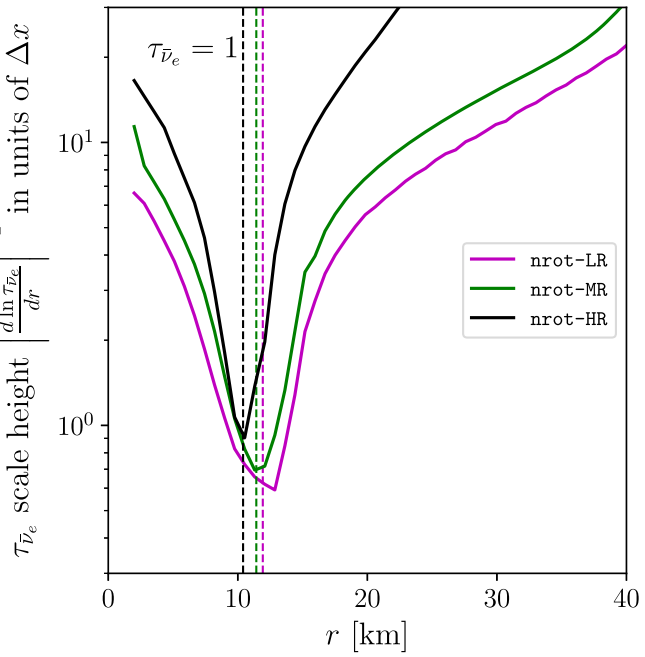

Figure 1. Scale height $H = \left|\frac{d\ln\tau_{\bar{\nu}_e}}{dr}\right|^{-1}$ associated with the $\bar{\nu}_e$ optical depth $\tau_{\bar{\nu}_e}$, as a function of radius r from the center of the PNS (solid lines), averaged over polar angle ($\theta = 0°$–$90°$) and time averaged from 50 to 100 ms for our three nonrotating PNS solutions with different spatial resolution: nrot−MR (black, $\Delta x \simeq 450$ m), nrot−LR (purple, $\Delta x \simeq 620$ m), and nrot−HR (green, $\Delta x \simeq 225$ m). None of the simulations resolve the region around the neutrinosphere radius ($\tau_{\bar{\nu}_e} = 1$; vertical dashed lines) with several grid points, and hence cannot accurately converge on the neutrino luminosity or mean energy. However, the gain region of net heating and wind zone on larger scales is well resolved by even the lowest resolution runs.

resolution that is approximately a factor of 10 higher than the highest resolution run we have explored (`nrot-HR`, with $\Delta x \simeq 225$ m), which is computationally infeasible for this study. As discussed below, we therefore do not (nor would we expect to) obtain convergent values for the steady-state neutrino luminosities or mean energies (Figures 4 and 8), as these are determined near the decoupling surface. However, this deficiency is not critical for the purposes of this study, because the neutrino radiation field serves primarily as a boundary condition controlling the wind heating and compositional changes at larger radii above the neutrinosphere: regions that are properly resolved. For example, our fiducial simulation nrot−HR resolves the temperature scale height in the decoupling region with at least four to five points while obtaining reasonably convergent hydrodynamic wind properties. Furthermore, as discussed in Section 3, the key wind properties (e.g., mass-loss rate, entropy) obtained by our nonrotating PNS simulations performed at lower spatial resolution than the fiducial model (nrot−MR and nrot−LR, respectively) do agree with one another to $\lesssim$10%, once the impact of their different neutrino luminosities and energies are accounted for as predicted by analytic scaling relations (Qian & Woosley 1996).

In order to reduce computational costs, we make use of appropriate symmetries and limit the computational domain to one quadrant of the full 4π–three-dimensional domain. For our rotating models, the z-axis corresponds to the rotational axis; thus for all models, we employ 180° rotational symmetry around the z-axis, as well as reflection symmetry across the xy-plane.

On physical grounds, we do not expect these symmetries to have an appreciable impact. For example, the wind entropy gradient in the gain layer is positive (see Figure 3(f)) and thus large-scale convective instabilities do not arise. Furthermore, our stellar models are not differentially rotating and have sufficiently low ratios of rotational energy to gravitational binding energy ($T/|W|$; see Table 1), so that they do not develop non-axisymmetric instabilities. To ensure that indeed our results do not depend on the choice of symmetry, we performed one of our rotating simulations with and without imposing symmetry (simulating the full 4π-three-dimensional domain for about 10 ms), finding indistinguishable results in the two cases.

Weak interactions and approximate neutrino transport are included via a leakage scheme (Bruenn 1985; Ruffert et al. 1996) following the implementation of Galeazzi et al. (2013) and Radice et al. (2016) as described in Siegel & Metzger (2018), together with a "ray-by-ray" transport scheme ("M0" scheme; Radice et al. 2016, 2018). The M0 scheme represents an approximation to neutrino transport derived by taking the first moment of the Boltzmann equation and using a closure relation that assumes neutrinos stream along radial rays at the speed of light. Neutrino mean energies and number densities are evolved according to radial evolution equations (Equations (A11) and (A15) of Radice et al. 2016). This ray-by-ray transport scheme does not account for potential neutrino interactions between different rays (i.e., lateral transport). The M0 transport scheme will be least accurate in regions of high optical depth, i.e., within the PNS for our study. As a result, the neutrino properties within the PNS may not be fully consistent with the temperature profile. However, in this region, we initiate a somewhat ad hoc radial temperature profile (Section 2.2), rather than one based on a self-consistent evolution (e.g., from the stellar core collapse or neutron star merger). In the spirit of previous work (e.g., Thompson et al. 2001) our primary goal is instead to characterize the properties of the resulting wind at a given neutrino luminosity and mean energy. Thus, the radial approximation should be sufficient because the wind is launched above the surface of the PNS where the optical depth is low, and is furthermore roughly spherically symmetric, even in the fastest rotating models.

The leakage scheme includes charged-current β-processes, electron-positron pair annihilation, and plasmon decay. Neutrino opacities include neutrino absorption by nucleons and coherent scattering on free nucleons and heavy nuclei. We neglect the effects of magnetic fields on the neutrino opacities, which is a good approximation except unless the PNS is extremely highly magnetized (e.g., Beloborodov 2003; Duan & Qian 2004). Optical depths are calculated using the quasi-local scheme presented by Neilsen et al. (2014).

The neutrino evolution is coupled to the equations of GRHD in an operator-split fashion, leading to electron fraction changes as well as neutrino energy and momentum deposition to matter. The dominant weak reactions for heating the wind and changing the electron fraction are

$$\nu_e + n \longleftrightarrow e^- + p \quad \text{and} \quad \bar{\nu}_e + p \longleftrightarrow e^+ + n, \tag{1}$$

where ν_e and $\bar{\nu}_e$ are the electron neutrino and anti-neutrino, p is the proton, n is the neutron, and e^- and e^+ are the electron and positron, respectively.

Neutrino energies and number densities are evolved on radial rays that represent a uniform spherical "M0 grid" extending

Table 1
Suite of 1.4 $M_\odot$ PNS Simulations

Model	R_e[a] (km)	P[b] (ms)	R_p/R_e[c]	$T/\lvert W\rvert$[d]	Ω/Ω_K[e]	$R_{\bar{\nu}_e}$[f] (km)	$\langle L_{\nu_e}\rangle$[g] (erg s^{-1})	$\langle L_{\bar{\nu}_e}\rangle$[h] (erg s^{-1})	$\langle E_{\nu_e}\rangle$[i] (MeV)	$\langle E_{\bar{\nu}_e}\rangle$[j] (MeV)
nrot-LR	12.7	n/a	1	0	0	12.1	5.3e51	8.5e51	12.5	18.0
nrot-MR	12.7	n/a	1	0	0	11.4	4.1e51	6.7e51	13.3	17.8
nrot-HR[k]	12.7	n/a	1	0	0	10.5	2.5e51	4.2e51	12.8	18.3
rot.9-MR	13.4	1.78	0.9	2.6e-2	0.40	10.5–11.7	2.9e51	4.4e51	12.5	18.4
rot.7-MR	15.7	1.15	0.7	7.8e-2	0.75	9.8–16.4	3.3e51	5.2e51	12.0	17.1
rot.6-MR	17.6	1.11	0.6	9.4e-2	0.94	10.0–17.5	3.0e51	4.9e51	11.7	17.0

Notes.
[a] Initial equatorial radius.
[b] Spin period.
[c] Initial ratio of polar to equatorial radius.
[d] Ratio of total rotational energy to gravitational binding energy.
[e] Ratio of rotational frequency to Keplerian frequency at stellar equator, $\Omega_K = \sqrt{GM/R_e^3}$.
[f] Steady-state radius of the anti-electron neutrinosphere (or range of radii, in rotating cases).
[g] Luminosities and mean energies of electron neutrinos and antineutrinos, averaged over the final factor of three in simulation time. Model names ending in HR, MR, LR have smallest box resolutions of 225, 450, and 620 m, respectively.
[h] Luminosities and mean energies of electron neutrinos and antineutrinos, averaged over the final factor of three in simulation time. Model names ending in HR, MR, LR have smallest box resolutions of 225, 450, and 620 m, respectively.
[i] Luminosities and mean energies of electron neutrinos and antineutrinos, averaged over the final factor of three in simulation time. Model names ending in HR, MR, LR have smallest box resolutions of 225, 450, and 620 m, respectively.
[j] Luminosities and mean energies of electron neutrinos and antineutrinos, averaged over the final factor of three in simulation time. Model names ending in HR, MR, LR have smallest box resolutions of 225, 450, and 620 m, respectively.
[k] Fiducial nonrotating wind model shown in Figures 2, 3.

radially to 200 km, with $n_r \times n_\theta \times n_\phi = 600 \times 20 \times 40$ grid points. As neutrino transport quantities only slowly change in time with respect to the hydro time step, and for computational efficiency, effective neutrino absorption is updated via M0 only every 16 time steps of the hydro evolution. Neutrino transport includes three neutrino species: electron neutrinos and antineutrinos (ν_e, $\bar{\nu}_e$), as well as all μ and τ neutrinos and antineutrinos grouped into one additional category (ν_x). The grid covers the neutrinosphere (for all species), defined by the surface above which the neutrino optical depth to infinity lies between 0.7 and 1, and the gain layer, where net neutrino heating unbinds matter from the PNS surface. The grid also extends to large enough radii to cover all densities for which weak interactions are expected to be appreciable ($\rho \gtrsim 10^4$ g cm^{-3}).

2.2. Neutron Star Models and Initial Conditions

For initial conditions, we construct axisymmetric hydrostatic profiles of nonrotating and solid-body rotating neutron stars of gravitational mass 1.4 $M_\odot$ with the RNS code (Stergioulas & Friedman 1995). Our grid of simulations, and the key properties of the PNS for each model, are summarized in Table 1.

For the equation of state (EOS), we adopt the SFHo[6] model (Steiner et al. 2013), which covers particle densities from 10^{27} to 10^{40} cm^{-3} and temperatures from 0.1 to 160 MeV. The EOS parameters are calibrated to nuclear binding energies as well as to other observational and experimental constraints. For densities below saturation density, the model accounts for light and heavy nuclei formation, and smoothly transitions from nuclei to uniform nuclear matter with a thermodynamically consistent excluded volume description (Hempel & Schaffner-Bielich 2010). A distribution of different nuclear species are assumed, rather than just the single-nuclei approximation. Results for light nuclei are in agreement with quantum many-body models. The presence of nuclei ensures that nuclear binding energy released as individual nucleons recombine into light nuclei is captured by the flow; conversion of this energy into kinetic energy can significantly affect the unbinding of winds (cf. Section 3). For this EOS, the radius of a 1.4 $M_\odot$ nonrotating cold neutron star is 11.88 km and the maximum stable mass is 2.059 $M_\odot$.

The initial temperature profile of the star as a function of density, $T(\rho)$, must be specified as an initial condition. Although our goal is to study PNS winds generated following a core-collapse supernova (or, potentially, a neutron star merger), we do not obtain the initial temperature profiles directly from supernova or merger simulations. Rather, we specify $T(\rho)$ as an ad hoc functional form following Kaplan et al. (2014), the parameters of which are so chosen to generate steady-state neutrino emission properties from the star similar to those predicted a few seconds after a successful core-collapse explosion (e.g., Pons et al. 1999) or neutron star merger event (e.g., Dessart et al. 2009). Specifically, we adopt a temperature profile that smoothly transitions from the hot PNS core temperature $T_{\rm max}$ to a colder atmosphere temperature $T_{\rm min}$ (Equation (A1) of Kaplan et al. 2014):

$$T(\rho) = T_{\rm min} + \frac{T_{\rm max}}{2}\left(\tanh\frac{(\log_{10}(\rho) - \bar{m})}{\bar{s}} + 1\right), \qquad (2)$$

where $\bar{m}$ is the midpoint of the logarithmic density roll off and $\bar{s}$ is the e-folding scale. We use the temperature profile denoted C20p0 in Kaplan et al. (2014), with parameters set as follows: $\bar{m} = 14.2$, $\bar{s} = 0.3$, $T_{\rm min} = 0.015$ MeV, and $T_{\rm max} = 20$ MeV.

[6] Available in tabulated form on stellarcollapse.org.

These parameter values were chosen to give rise to approximate target values of the neutrino luminosities and mean energies, once a steady wind has been established.

As with the temperature profile, the initial electron fraction profile $Y_e(\rho, T)$ must be specified. Given the EOS and temperature profile, we again follow Kaplan et al. (2014) and set

$$Y_e(\rho, T[\rho]) = Y_{e,\nu-\mathrm{free}\beta}(\rho)(1 - e^{-\rho_{\mathrm{trap}}/\rho}) + Y_{e,\nu-\mathrm{trap}\beta}(\rho, T[\rho])e^{-\rho_{\mathrm{trap}}/\rho}, \quad (3)$$

where $Y_{e,\nu-\mathrm{free}\beta}$ denotes the electron fraction for cold matter in β equilibrium without neutrinos (computed at T_{min}) and $Y_{e,\nu-\mathrm{trap}\beta}$ refers to the electron fraction for hot and dense matter in β equilibrium with neutrinos present. For densities $\rho \ll \rho_{\mathrm{trap}} \sim 10^{12.5}\,\mathrm{g\,cm^{-3}}$, neutrinos decouple from matter. To account for free-streaming neutrinos near the PNS surface ($\rho \lesssim \rho_{\mathrm{trap}}$), the attenuation factor $e^{-\rho_{\mathrm{trap}}/\rho}$ serves to smoothly connect the hot and cold matter solutions.

The function $Y_{e,\nu-\mathrm{free}\beta}$ in Equation (3) is obtained from the EOS according to the condition

$$\mu_\nu = 0 = \mu_p - \mu_n + \mu_e, \quad (4)$$

at T_{min}, where μ_ν, μ_n, μ_p, μ_e are the chemical potentials of the neutrinos, neutrons, protons, and electrons, respectively. As the neutrino density n_ν is negligible in the free-streaming regions, the lepton fraction (ratio of lepton to baryon number) obeys $Y_{\mathrm{lep}} = Y_{e,\nu-\mathrm{free}\beta}$.

We calculate $Y_{e,\nu-\mathrm{trap}\beta}$ by treating neutrinos as a relativistic Fermi gas in equilibrium, computing the neutrino fraction Y_ν according to

$$Y_\nu = \frac{n_\nu}{\rho N_A}, \quad (5)$$

where n_ν is obtained from Fermi integral relations (Equation (B5) of Kaplan et al. 2014). We then iteratively solve the relation

$$0 = Y_{\mathrm{lep}} - (Y_{e,\nu-\mathrm{trap}\beta} + Y_\nu), \quad (6)$$

where Y_{lep} is computed from Equation (4), used here as a fixed input. The value of Y_e dictated by this prescription is roughly constant for $\rho \lesssim 10^7\,\mathrm{g\,cm^{-3}}$ (corresponding to the "atmosphere" on the simulation grid), so we initialize $Y_e(\rho \lesssim 3 \times 10^6\,\mathrm{g\,cm^{-3}})$ to $Y_{\mathrm{atm}} \approx 0.46$. Likewise, we set the density and temperature of the initial atmosphere to $\rho_{\mathrm{atm}} = 340\,\mathrm{g\,cm^{-3}}$ and $T_{\mathrm{atm}} = 0.\,015\,\mathrm{MeV}$, respectively.

Stellar models are computed using `RNS`, which solves the general-relativistic Euler equations for a uniformly rotating star in axisymmetric spacetime (Stergioulas & Friedman 1995). In specifying the EOS, `RNS` requires a table of the energy density as a function of pressure. We generate this table over the relevant range of densities using the EOS with the temperature and Y_e prescriptions from above. A stellar model is constructed by specifying a central density ρ_c and a polar to equatorial radius axis ratio R_p/R_e. For solutions with arbitrary rotation frequency, `RNS` first integrates the TOV equations and finds a nearest solution. The code then estimates solutions through an iterative procedure until the desired ratio R_p/R_e is achieved. For the nonrotating models, the radius of the neutron star is found to be $R_e = R_p = 12.70$ km, larger than the equivalent cold radius of 11.88 km and consistent with the temperature-dependent PNS radius found by Kaplan et al. (2014).

For our most rapidly rotating model, `rot.6-MR`, we adopt a PNS rotating near break-up, with $\Omega/\Omega_K \approx 0.944$, where Ω_K is the Keplerian orbital frequency, corresponding to an axis ratio $R_p/R_e = 0.6$ ($R_e \simeq 17.6$ km) and spin period $P \approx 1.11$ ms. We also run two cases of intermediate rotation, $R_p/R_e = 0.7$ (`rot.7-MR`; $P = 1.15$ ms) and $R_p/R_e = 0.9$ (`rot.9-MR`; $P = 1.78$ ms). Further details on the models are given in Table 1.

2.3. Conditions for r-process Nucleosynthesis

Before describing the results of our simulations, we briefly review the physical processes in the PNS wind that determine whether a successful r process can take place. The surface of the PNS and the inner regions of the wind are sufficiently hot that protons and neutrons exist as free nucleons. Free nuclei recombine into α particles at radii in the wind where the temperature decreases to $T \lesssim 5 \times 10^9$ K, as typically occurs ∼50−100 km above the PNS surface in our models (cf. Figures 2 and 5). Heavier elements then begin to form as the temperature decreases further, starting with the reaction $^4\mathrm{He}(\alpha\mathrm{n},\gamma)^9\mathrm{Be}(\alpha,\mathrm{n})^{12}\mathrm{C}$ for $Y_e \lesssim 0.5$. After ^{12}C forms, additional α-particle captures produce heavy seed nuclei with characteristic mass $\bar{A} \approx 90 - 120$ and charge $\bar{Z}$ ("alpha-process"; e.g., Woosley & Hoffman 1992). Finally, the r process itself occurs, as the remaining free neutrons (if any) capture onto these seed nuclei.

The maximum atomic mass A_{max} to which the r process can proceed depends on the ratio of free neutrons to seed nuclei following the completion of the α process. Because ^{12}C-formation is the rate-limiting step to forming the seeds, the neutron-to-seed ratio (and hence A_{max}) depends on the electron fraction Y_e, asymptotic wind entropy s_∞, and expansion time τ_{exp} through the seed-formation region (Hoffman et al. 1997; Meyer & Brown 1997). We follow Hoffman et al. (1997) in defining the latter as[7]

$$\tau_{\mathrm{exp}} \equiv \frac{1}{v^r}\left|\frac{d\ln T}{dr}\right|^{-1}_{\mathrm{T\,=\,0.5MeV}}. \quad (7)$$

For $\bar{Z}/\bar{A} \approx 0.35 - 0.4 \lesssim Y_e \lesssim 0.5$, the condition for the r process to reach the second or third peak can be expressed as[8]

$$\eta \equiv \frac{s_\infty^3}{Y_e^3 \tau_{\mathrm{exp}}} \gtrsim \eta_{\mathrm{thr}} \approx \begin{cases} 4 \times 10^9 & \text{if } A_{\mathrm{max}} \sim 135 \text{ (second peak)} \\ 9 \times 10^9 & \text{if } A_{\mathrm{max}} \sim 195 \text{ (third peak)} \end{cases}, \quad (8)$$

where s_∞ is expressed[9] in k_b baryon^{-1} and τ_{exp} in seconds. Thus, the ratio η/η_{thr} serves as a "figure of merit" for the potential success of a given r-process site in the $0.4 \lesssim Y_e \lesssim 0.5$ regime.

Previous studies of the r process in spherical nonrotating PNS winds typically find $\eta \ll \eta_{\mathrm{thr}}$, thus disfavoring these

[7] Thompson et al. (2001) define a similar quantity, but in terms of the gradient of the density profile rather than the temperature ($\tau_{\mathrm{exp},\,\rho}$). Given that entropy obeys $s \propto T^3/\rho$ for a radiation-dominated plasma and that s is roughly constant in the wind outside the gain region, it follows that $\tau_{\mathrm{exp}} \approx 3\ \tau_{\mathrm{exp},\rho}$.

[8] The combination s^3/τ_{exp} enters because the abundance of ^{12}C nuclei (and hence the number of seed nuclei) created in the wind is equal to an integral of the effective four-body $^4\mathrm{He}(\alpha n,\gamma)^9\mathrm{Be}(\alpha,n)^{12}\mathrm{C}$ reaction rate $\propto \rho^3$ times the timescale available for formation $\propto \tau_{\mathrm{dyn}}$; for radiation-dominated conditions, $s \propto T^3/\rho$ and so $\rho \propto s^{-1}$ given that seed nuclei form at roughly a fixed temperature.

[9] Throughout the remainder of the paper, specific entropy is expressed in units of k_B baryon^{-1} for notational brevity.

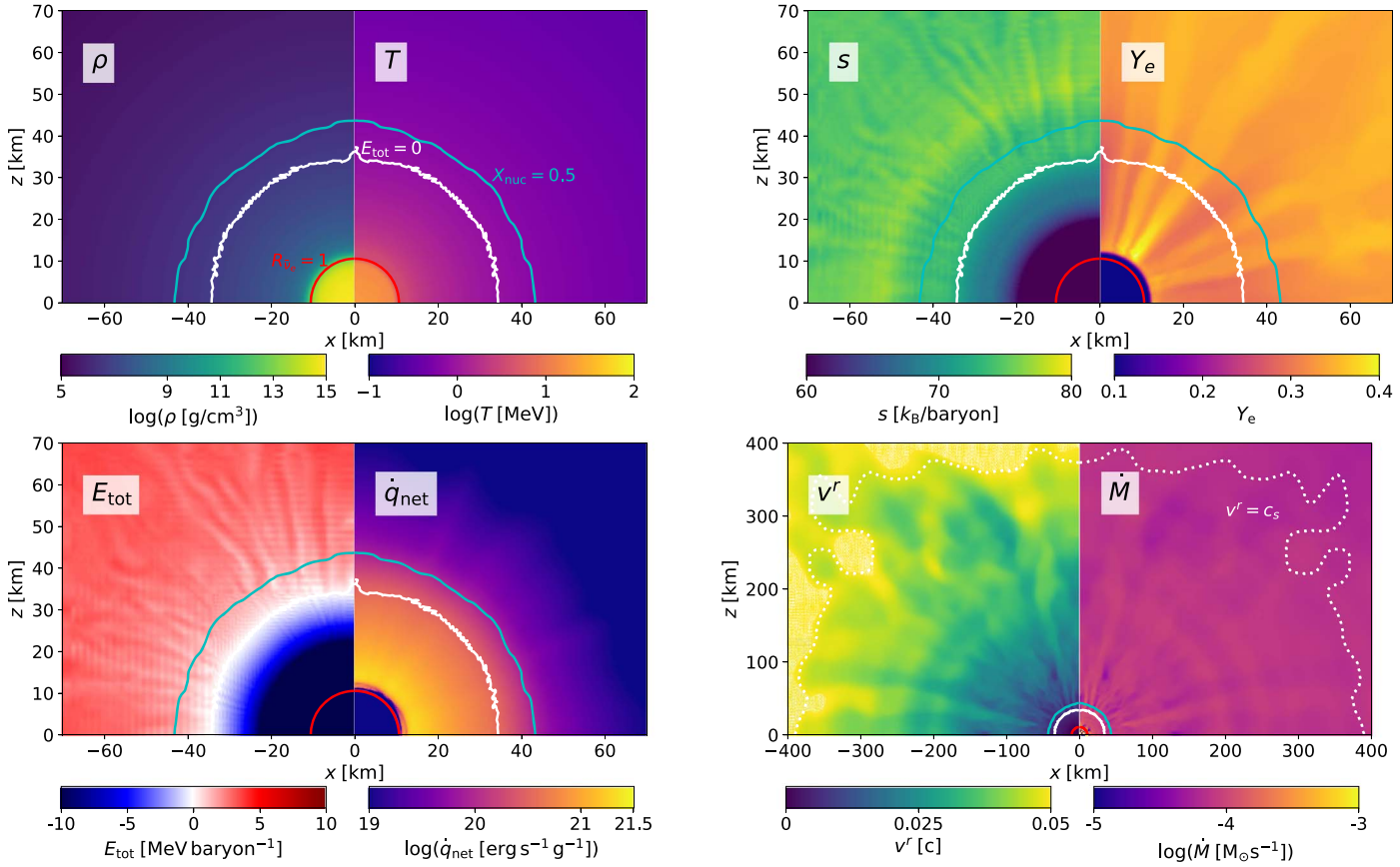

Figure 2. Snapshots of various quantities from our fiducial nonrotating model `nrot-HR` showing a slice through the $y = 0$ plane at $t = 152$ ms, with contours at the neutrinosphere ($\tau_{\bar{\nu}_e} = 1$; red), $E_{tot} = 0$ (white), the α-particle formation surface (teal; X_{nuc} refers to the mass fraction of all nuclei excluding individual nucleons), and the sonic surface (where $v^r = c_s$; white dotted line). The top left panel shows the density ρ and temperature T. The top right panel shows the specific entropy s and the electron fraction Y_e. The bottom left panel shows E_{tot}, the total specific energy of wind matter as measured at infinity ($E_{tot} = -hu_t - 1$, where h is the specific enthalpy and u_t is the time component of the four-velocity u), and the net neutrino heating rate $\dot{q}_{net}$. The bottom right panel shows the radial velocity v^r and the isotropic-equivalent mass-loss rate $\dot{M}$. Please note the different radial scale on the bottom right subpanel compared to the other subpanels.

events as sources of heavy r-process nuclei unless $Y_e \ll 0.4$. Furthermore, if $Y_e > 0.5$, as suggested by some recent cooling calculations of nonrotating PNS (e.g., Pascal et al. 2022), then an r process will not be achieved for any value of η (however, see Meyer 2002 for an exception).

On the other hand, if $Y_e < \bar{Z}/\bar{A} \sim 0.35 - 0.4$, then an r process is possible for $\eta \ll \eta_{thr}$, with third-peak element production occurring for $Y_e \lesssim 0.25$ (Lippuner & Roberts 2015). The latter is the regime encountered in the dynamical and disk wind ejecta of neutron star mergers (e.g., Freiburghaus et al. 1999; Siegel & Metzger 2017) and, potentially, the winds from rapidly spinning proto-magnetars (e.g., Metzger et al. 2007, 2018).

3. Results

3.1. Nonrotating PNS Wind

Figures 2–4 illustrate our results for the fiducial nonrotating model `nrot-HR`. Figure 2 shows snapshots through the meridional ($y = 0$) plane of various quantities near the end of the simulation at $t = 152$ ms, once the wind has achieved an approximate steady state (defined such that the asymptotic wind properties have reached a state of being approximately radially and temporally constant). Figure 3 shows angle-averaged radial profiles of the density ρ, temperature T, radial velocity v^r, net specific heating rate $\dot{q}_{net}$, mass-loss rate $\dot{M}$, specific entropy s, and electron fraction Y_e at different snapshots in time, starting from $t \approx 30$ ms and going through to the end of the simulation at $t \approx 142$ ms. The net specific heating rate is given by

$$\dot{q}_{net} = \dot{q}^+ - \dot{q}^- = \sum_{\nu_e, \bar{\nu}_e} \kappa_{\nu_i} (n_{\nu_i}/\rho) E_{\nu_i} - \sum_{\nu_i} \dot{q}^{eff}_{\nu_i}, \quad (9)$$

where κ_{ν_i}, n_{ν_i}, and E_{ν_i} denote the neutrino opacities, number densities, and mean energies, respectively, and $\dot{q}^{eff}_{\nu_i}$ are the total specific cooling rates for each neutrino species $\nu_i = \{\nu_e, \bar{\nu}_e, \nu_X\}$. Here, ν_X collectively labels the heavy-lepton neutrinos and antineutrinos. The time evolution of the outflowing wind properties, angle-averaged across a spherical surface of radius 60 km, are shown in Figure 4.

After a transient phase, the density profile close to the PNS surface settles into an exponentially declining profile of a hydrostatic atmosphere, which then transitions at larger radii to a more gradual power-law decline characteristic of a wind (Figures 2, 3). The $\bar{\nu}_e$ neutrinosphere is indicated by a red line and a red dashed vertical line in Figures 2 and 3, respectively.

The radial profiles of the matter density, temperature, and net specific neutrino heating rate ($\dot{q}_{net} = \dot{q}^+ - \dot{q}^-$; heating minus cooling) settle into an approximate steady state by $t \approx 68$ ms (Figures 2, 3(a)–(c)). By this time, the neutrino luminosities and energies also stabilize (Figure 4, middle row), with $L_{\nu_e} \approx 2.5 \times 10^{51}$ erg s^{-1}, $L_{\bar{\nu}_e} \approx 4.2 \times 10^{51}$ erg s^{-1},

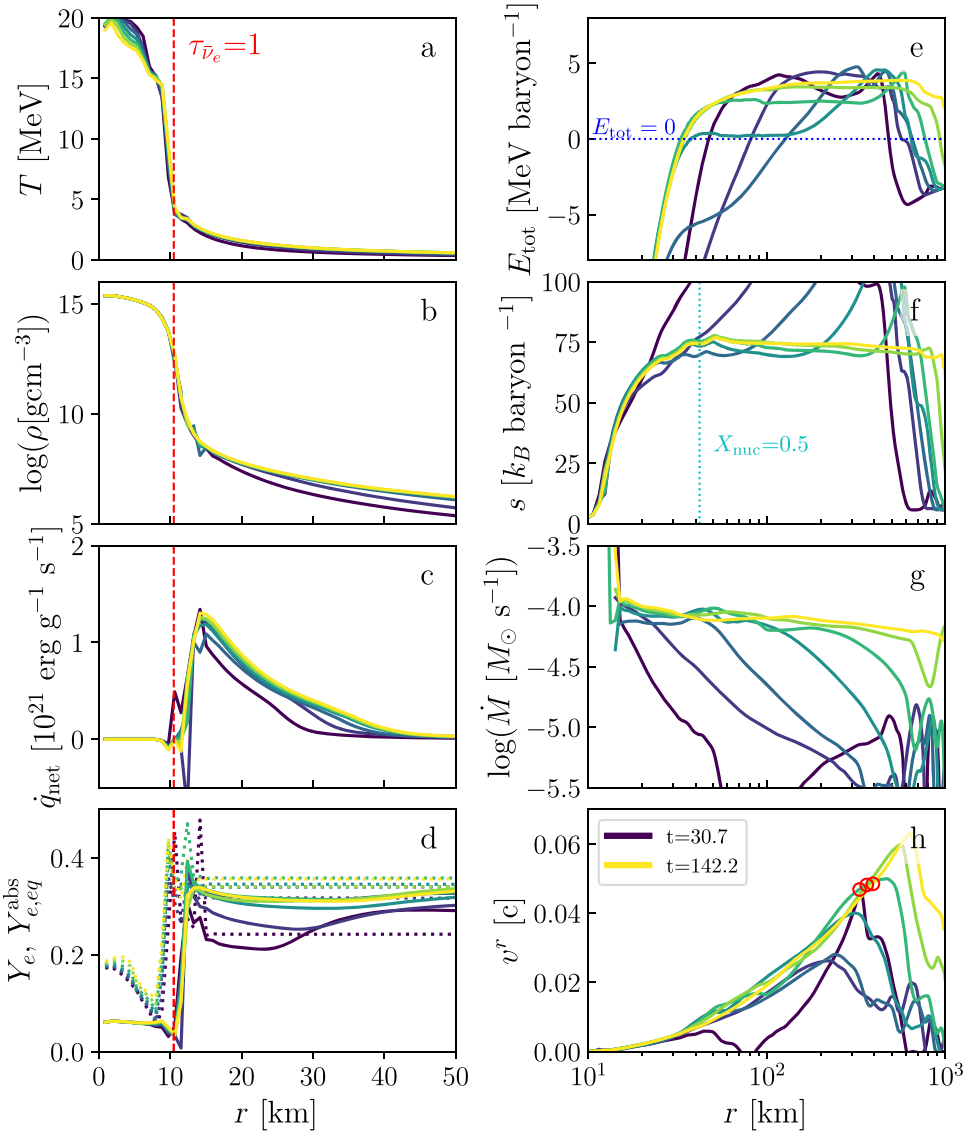

Figure 3. Radial profiles of angle-averaged quantities for model `nrot-HR` at several times (from dark to light): $t = 30$, 49, 68, 87, 105, 124, and 142 ms. Plotted are (a) temperature, T; (b) mass density, ρ; (c) net specific neutrino heating rate, $\dot{q}_{\rm net}$; (d) electron fraction, Y_e (solid), and limited equilibrium electron fraction $Y^{\rm abs}_{e,\rm eq}$ (dotted); (e) total specific energy, $E_{\rm tot}$; (f) specific entropy, s; (g) mass outflow rate, $\dot{M}$; (h) radial velocity, v^r. The red vertical dashed line denotes the location of the $\bar{\nu}_e$ neutrinosphere. The $\tau_{\bar{\nu}_e}$=1 and α-formation surface ($X_{\rm nuc} = 0.5$, where $X_{\rm nuc}$ is the mass fraction of all nuclei excluding individual nucleons) at $t = 152$ ms (corresponding to the snapshot in Figure 2) are indicated by red dashed and teal dotted lines in panels (a)–(d) and (f), respectively. Red circles denote the sonic surface at which the radial velocity v^r equals the sound speed; there are only three such circles because the sonic surface does not enter the grid until the final three snapshots. Please note the different radial scales for quantities shown in the left and right columns.

$E_{\nu_e} \approx 13$ MeV, and $E_{\bar{\nu}_e} \approx 18$ MeV (Table 1). Over this same period, the radius of the neutrinosphere (taken to be that of $\bar{\nu}_e$) grows from ≈10 km to 10.5 km. These PNS luminosities and radii correspond to those achieved on timescales of a few seconds after a successful core-collapse supernovae (e.g., Pons et al. 1999; Scheck et al. 2006; Roberts et al. 2012), the same epoch over which the bulk of the total PNS mass loss occurs.

Close to the PNS surface, heating from neutrino captures balance cooling from pair captures (Equation (1)). Moving above the surface, the temperature drops (Figures 2, 3(a)) and neutrino cooling from pair captures on nuclei ($\dot{q}^- \propto T^6$) plummets, while the heating rate $\dot{q}^+$ remains roughly constant with radius. Consequently, a "gain layer" of net neutrino heating $\dot{q}_{\rm net} = \dot{q}^+ - \dot{q}^- > 0$ forms at radii $r \sim 10$–50 km (Figure 2, 3(c)). This heating causes the entropy of the outflowing material to rise, $s = \int dq/T$, in the gain layer and then plateau at larger radii to $s \simeq 74$ (Figure 2, 3(f)).

The α-particle formation surface lies at $r \approx 45$ km, where the temperature has dropped to ≈0.5–0.7 MeV. We define this surface here as that beyond which the mass fraction $X_{\rm nuc}$ of all nuclei excluding individual nucleons becomes larger than 50%. Heat released during α recombination reactions introduces an increase in the wind entropy, which can be seen as the bright ring in the top right panel of Figure 2, or the fluctuations at $r = 30$–60 km in the entropy radial profiles of Figures 2, 3(f).

Radiation pressure dominates over gas pressure in the high-entropy outflow near and above the gain layer, and the resulting radial pressure gradient causes material to accelerate outwards. The radial velocity, plotted in Figures 2, 3(h), increases with radius. Material becomes unbound from the PNS around $r \approx 30$–40 km, as indicated by a positive total specific energy $E_{\rm tot} = -hu_t - 1$ (Figures 2 and 3(e)).

By $t \approx 105$ ms, a sonic surface, at which the radial velocity equals the sound speed, has been established around $r = 300$ km

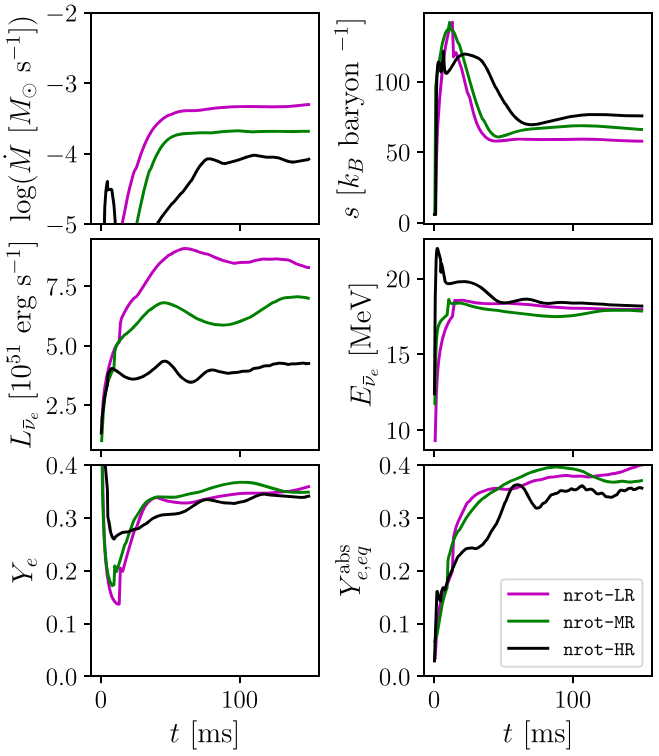

Figure 4. Time evolution of angle-averaged wind properties (as measured through an $r = 60$ km spherical surface) for the nonrotating models of low resolution `nrot-LR` (purple), medium resolution `nrot-MR` (green), and high resolution `rot-HR` (black). Asymptotic wind properties such as the mass-loss rate and specific entropy are not converged with resolution because the neutrino decoupling region which sets the neutrino radiation field is not resolved (Figure 1). However, when the wind properties are scaled following the Qian & Woosley (1996) analytic formulae to results from one-dimensional time-independent models Thompson et al. (2001), or to each another, based on their respective neutrino luminosities/energies/neutrinosphere radii, they come into better agreement (Table 3).

(denoted by red circles in Figure 3(h)). By the end of the simulation, the sonic surface is approaching ≈400 km (see also Figure 2) and the wind has attained a velocity $v \gtrsim 0.06\,c$. The sonic radius agrees with those found by Thompson et al. (2001) for similar wind parameters. Though the wind is still accelerating, its total energy $E_{\rm tot}$ has plateaued to a value ≈3 MeV per baryon, which will translate (once the enthalpy is converted into bulk kinetic energy) into an asymptotic speed $v_\infty \equiv \sqrt{2E_{\rm tot}} \approx 0.09\,c$. By the final snapshot, the mass-loss rate approaches the radially constant profile expected of a steady-state wind (Figures 2, 3(g)), reaching an asymptotic value $\dot{M} \approx 3.2 \times 10^{-4}\,M_\odot\ {\rm s}^{-1}$.

Absorption of neutrinos by the wind material also causes the electron fraction Y_e to rise with radius from its low value near the neutrinosphere (Figure 4, bottom row). Neglecting relativistic effects, the electron fraction in an outflowing fluid element evolves according to the reactions in Equation (1),

$$\frac{dY_e}{dt} = (\lambda_{e^+} + \lambda_{\nu_e})(1 - Y_e) - (\lambda_{e^-} + \lambda_{\bar{\nu}_e})Y_e, \tag{10}$$

where λ_{e^+} and λ_{ν_e} are the positron and electron neutrino capture rates on neutrons, and λ_{e^-} and $\lambda_{\bar{\nu}_e}$ are the electron and electron anti-neutrino capture rates on protons, respectively. The equilibrium electron fraction at any location can be defined as the value $Y_e = Y_e^{\rm eq}$ for which $dY_e/dt = 0$. This equilibrium is approached on the characteristic timescale,

$$\tau_\beta = \frac{1}{(\lambda_{e^+} + \lambda_{\nu_e})(1 - Y_e) + (\lambda_{e^-} + \lambda_{\bar{\nu}_e})Y_e}. \tag{11}$$

Near the PNS surface, where the radial velocity is low, τ_β is much shorter than the expansion time of the outflow ($\tau_{\rm exp} \sim \rho/\dot{\rho}$) and hence $Y_e \simeq Y_e^{\rm eq}$ is well satisfied. However, as the wind accelerates at larger radii, $\tau_{\rm exp}$ decreases, until eventually $\tau_\beta \gtrsim \tau_{\rm exp}$, causing Y_e to freeze out.

In PNS winds, the temperatures are sufficiently low by the radii at which Y_e freeze-out occurs that the pair capture reactions (λ_{e^+}, λ_{e^-}) are negligible compared to the neutrino absorption reactions (λ_{ν_e}, $\lambda_{\bar{\nu}_e}$). Thus, around the point of freeze-out, a limited equilibrium has been achieved, in which ν_e absorption reactions on protons balance $\bar{\nu}_e$ absorption reactions on neutrons.[10] The electron fraction corresponding to this limited equilibrium, $Y_{e,{\rm eq}}^{\rm abs}$, depends exclusively on the $\nu_e/\bar{\nu}_e$ neutrino radiation fields (Qian et al. 1993; Qian & Woosley 1996), viz.

$$\begin{aligned} Y_{e,{\rm eq}}^{\rm abs} &\simeq \frac{\lambda_{\nu_e}}{\lambda_{\nu_e} + \lambda_{\bar{\nu}_e}} \\ &\approx \left(1 + \frac{L_{\bar{\nu}_e}}{L_{\nu_e}} \frac{\langle \epsilon_{\bar{\nu}_e} \rangle - 2\Delta + 1.2\Delta^2/\langle \epsilon_{\bar{\nu}_e} \rangle}{\langle \epsilon_{\nu_e} \rangle - 2\Delta + 1.2\Delta^2/\langle \epsilon_{\nu_e} \rangle}\right)^{-1}, \end{aligned} \tag{12}$$

where $\Delta \equiv m_n - m_p \simeq 1.293$ MeV is the proton–neutron mass difference and $\langle \epsilon_\nu \rangle = \langle E_\nu^2 \rangle / \langle E_\nu \rangle$ is the corresponding mean neutrino energy.

Figure 3(d) shows that the nonrotating PNS wind achieves $Y_e < Y_{e,{\rm eq}}^{\rm abs}$ near the PNS surface at early times, but that Y_e approaches $Y_{e,{\rm eq}}^{\rm abs}$ at large radii and late times. At larger radii $r \gtrsim$ 15 km, both $Y_{e,{\rm eq}}^{\rm abs}$ and Y_e are roughly constant with radius, as expected since the neutrino radiation field is fixed well above the neutrinosphere and weak interactions have frozen out, respectively.

Figure 4 (bottom row) shows that by $t \sim 100$ ms, $Y_{e,{\rm eq}}^{\rm abs}$ has settled close to a value of ∼0.35, with Y_e approaching this value as well, from below. These Y_e values are lower than predicted by detailed PNS cooling calculations at epochs of comparable neutrino luminosities to those of our solutions (e.g., Martínez-Pinedo et al. 2012; Roberts et al. 2012; Pascal et al. 2022); this is not surprising because our initial conditions are not based on the self-consistent outcome of a successful supernova and because the decoupling region which determines the neutrino luminosities and energies is not well resolved (Figure 1).

The black lines in Figure 7 show the time-averaged wind properties through two different spherical surfaces ($r = 60$, 120 km) as a function of polar angle θ with respect to the z-axis. With the exception of the isotropic neutrino luminosity right along the pole ($\theta = 0$), most of the wind quantities are roughly spherically symmetric and show no major effects of the

[10] The fact that $Y_e \simeq Y_{e,{\rm eq}}^{\rm abs}$ in PNS winds can also be understood from an energetic argument (e.g., Metzger et al. 2008): (1) the wind is unbound from the gravitational potential well of the PNS by neutrino heating; (2) because the gravitational binding energy per nucleon ∼200 MeV greatly exceeds the mean energy of the neutrinos absorbed by the wind material ≲20 MeV, each nucleon must absorb several neutrinos on average to become unbound; (3) from these multiple absorptions per nucleon, the wind necessarily "forgets" about the initial ratio of protons to neutrons on the PNS surface in favor of $Y_e^{\rm eq}$.

Table 2
Asymptotic Properties of Rotating and Nonrotating PNS Winds

Model	s_∞	Y_e	$\eta/\eta_{\rm crit}$ (Equation (8))	$\tau_{\rm exp}$	$\dot{M}$	v_∞[c]
…	[k_B baryon^{-1}]	…	…	[ms]	[$M_\odot$ s^{-1}]	[c]
nrot-HR	73.9	0.34	4.9×10^{-2}	21.5	7.40×10^{-5}	$\gtrsim$0.09
Thompson[d]	98.4	0.47	3.9×10^{-2}	23.79	1.63×10^{-5}	$\approx$0.08
nrot-HRscaled[e] to Thompson	85.1	0.47	1.9×10^{-2}	32.5	1.80×10^{-5}	…
rot.6-MR($0 \leqslant \theta \leqslant 180°$)	28.6	0.33	2.2×10^{-3}	31.1	1.19×10^{-3}	0.037
rot.6-MR (Polar[a])	56.9	0.35	1.4×10^{-2}	15.2	1.37×10^{-4}	0.096
rot.6-MR (Equatorial[b])	19.2	0.30	1.0×10^{-3}	49.3	6.09×10^{-4}	0.019

Notes. All quantities are averaged over the final third of the simulation run (e.g., 100–150 ms for nrot-HR).
[a] Averaged over $\theta \in [0, 30°]$ and $\theta \in [150°, 180°]$;
[b] Averaged over $\theta \in [60°, 120°]$;
[c] Asymptotic wind velocity, calculated from the total energy of the wind at large radii according to $v_\infty \equiv \sqrt{2E_{\rm tot}}$;
[d] From the $M = 1.4\,M_\odot$, $L_{\bar{\nu}_e} = 4 \times 10^{51}$ erg s^{-1} model of Thompson et al. (2001) (Row 6 of their Table 1);
[e] Expressions for entropy, mass-loss rate, and dynamical time obtained by rescaling the results of model nrot-HRto the neutrino luminosities, energies, and neutrinosphere radii of model Thompson following analytic expressions from Qian & Woosley (1996), e.g., $\dot{M} \propto \sum_{\nu=\nu_e,\bar{\nu}_e} L_\nu^{5/3} E_\nu^{10/3} R_\nu^{5/3}$; $s_\infty \propto \sum_{\nu=\nu_e,\bar{\nu}_e} L_\nu^{-1/6} E_\nu^{-1/3} R_\nu^{-2/3}$; $\tau_{\rm exp} \propto \sum_{\nu=\nu_e,\bar{\nu}_e} L_\nu^{-1} E_\nu^{-2} R_\nu$.

Table 3
Resolution Study of Nonrotating PNS Wind Properties

Model	s_∞	s_∞ (scaled)[b]	$\dot{M}$	$\dot{M}$ (scaled)[b]
…	[k_B baryon^{-1}]	[k_B baryon^{-1}]	[$M_\odot$ s^{-1}]	[$M_\odot$ s^{-1}]
Thompson[a]	98.4	…	1.63×10^{-5}	…
nrot-HR	73.9	85.1	7.40×10^{-5}	1.80×10^{-5}
nrot-MR	67.6	90.2	2.02×10^{-4}	2.00×10^{-5}
nrot-LR	58.7	85.0	3.71×10^{-4}	1.89×10^{-5}

Notes. Quantities are averaged over polar angle $\theta \in [0, 180°]$, and in time from $t = 100$ to 150 ms.
[a] From the $M = 1.4\,M_\odot$, $L_{\bar{\nu}_e} = 4 \times 10^{51}$ erg s^{-1} model of Thompson et al. (2001) (Row 6 of their Table 1).
[b] Entropy and mass-loss rate scaled to the Thompson model in the same way as described in Table 2.

grid boundaries, with $\dot{M}$ and v^r varying by factors of about two or less across all θ and the other quantities varying by $\lesssim$10%.

Table 2 summarizes the asymptotic wind properties, including $\dot{M}$, s_∞, Y_e, and v_∞. These are usefully compared to time-independent one-dimensional wind solutions available in the literature (e.g., Thompson et al. 2001). The closest model of Thompson et al. (2001) to our nonrotating models is their $M = 1.4\,M_\odot$ model with $L_{\nu_e} = 3.1 \times 10^{51}$ erg s^{-1}, $L_{\bar{\nu}_e} = 4 \times 10^{51}$ erg s^{-1}, for which they obtain $\dot{M} \approx 1.63 \times 10^{-5}\,M_\odot$ s^{-1}, $s_\infty \approx 98$, and $v_\infty \approx 0.08\,c$ (their Table 1; hereafter model Thompson). As summarized in Table 2, other than the value of Y_e (which is not expected to agree given the different $L_{\nu_e}/L_{\bar{\nu}_e}/E_{\nu_e}/E_{\bar{\nu}_e}$ values), the Thompson et al. (2001) wind properties broadly agree with those of our nonrotating PNS wind solutions. This agreement is further improved if the wind properties are scaled to ours using the analytic formulae of Qian & Woosley (1996) given our solutions' respective neutrino luminosities and energies.

To verify that our wind properties converge, we compare results from three otherwise similar nonrotating wind simulations with different resolutions in Figure 4. Figure 1 shows that we do not resolve the neutrino decoupling region in any of the models, as this would require a 10-fold increase in spatial resolution. As such, the predicted properties of the neutrino radiation field $\{L_{\bar{\nu}_e}, L_{\nu_e}, E_{\bar{\nu}_e}, E_{\nu_e}\}$ and the neutrinosphere radii $\{R_{\bar{\nu}_e}, R_{\nu_e}\}$ vary significantly between the models in Figure 4. However, after scaling the steady-state wind quantities $\dot{M}$ and s_∞ to the closest equivalent model of Thompson et al. (2001) and to each other based on their respective neutrino properties following the analytic formulae from Qian & Woosley (1996), the wind quantities come into approximate agreement (within tens of percent; Table 3).

The parameter $\eta = s_\infty^3/(Y_e^3 \tau_{\rm exp})$ (Equation (8)) quantifies the potential to form heavy r-process elements at large radii in the wind via the α-rich freeze-out mechanism (Section 2.3). Given the asymptotic wind entropy ($s_\infty \approx 74$) and expansion time through the seed-formation region ($\tau_{\rm exp} \approx 21.5$ ms) of our nonrotating model, this yields a value $\eta \approx 4.5 \times 10^8$ (Table 2), well below the threshold value $\eta_{\rm thr} \approx 9 \times 10^9$ to achieve even a second-peak r process (Equation (8)) for values of the electron fraction $Y_e \gtrsim \bar{Z}/\bar{A} \sim 0.4$ regime. The inability of spherically symmetric nonrotating purely neutrino-driven winds to yield a successful heavy r process is consistent with previous findings (see discussion and references in Section 1). The next subsection addresses whether these conclusions change in the presence of rapid rotation.

3.2. Rapidly Rotating PNS Winds

Rotation is expected to have a significant impact on the dynamics of the wind, at least in the equatorial regions of the flow, if the rotational velocity $v^{\phi} \sim R_{\nu}\Omega$ near the neutrinosphere radius R_{ν} exceeds the sound speed, c_s, in the gain region. Gas pressure dominates radiation pressure near the neutrinosphere at the base of the approximately isothermal gain layer ($s \sim P_{\rm rad}/P_{\rm gas} \gtrsim 1$; Figures 2, 3(f)), such that $c_s \simeq (kT/m_p)^{1/2}$. Approximating the single-species neutrino luminosity $L_{\nu} \simeq 4\pi(7/8)R_{\nu}^2\sigma T^4$ as that of a Fermi–Dirac blackbody, rotation will become dynamically important in the PNS atmosphere for spin periods $P = 2\pi/\Omega$ below a critical value (e.g., Thompson et al. 2004),

$$P_c \approx 2\pi\frac{R_{\nu}}{c_s} \approx 3.4\ {\rm ms}\left(\frac{R_{\nu}}{12\ {\rm km}}\right)^{5/4}\left(\frac{L_{\nu}}{10^{52}\ {\rm erg\ s^{-1}}}\right)^{-1/8}. \quad (13)$$

We focus our discussion on the most rapidly rotating model, `rot.6-MR`, with axis ratio $R_p/R_e = 0.6$ and spin period of $P = 1.11\ {\rm ms} \ll P_c$ (Table 1). Figure 5 shows two-dimensional snapshots of various kinematic and thermodynamic quantities in the meridional (x-z) plane for model `rot.6-MR` near the end of the simulation at $t = 100$ ms. Angular profiles (where θ is measured from the axis of rotation) of wind quantities through spherical surfaces of radius $r = 60$ km and $r = 120$ km are shown in Figure 7, comparing the results of `rot.6-MR` to those of the nonrotating model `nrot-HR` (for which the wind properties are expected and seen to be approximately uniform with angle).

Broadly speaking, our simulations reveal that the rotating wind can be divided into two angular regions with qualitatively distinct properties: (1) a fast polar outflow that develops quickly with properties across this region qualitatively similar to those of a nonrotating PNS; (2) a slower, denser equatorial outflow whose properties differ markedly from the nonrotating case, and which dominates the total mass-loss rate from the star.

After an initial transient phase, the density settles into an approximate steady state with an equatorial bulge of density $\rho \sim 10^{12}\ {\rm g\ cm^{-3}}$ extending out to a cylindrical radius $\varrho \approx 30$ km (Figure 5), compared to the steeper density profile along the polar axis, which falls to $\rho \lesssim 10^{8}\ {\rm g\ cm^{-3}}$ by $z \gtrsim 15$ km. The neutrinosphere surface is likewise oblate in shape, bulging out to $\varrho \approx 17$ km in the equatorial plane compared to $z \approx 10$ km along the polar axis (Figure 6), the latter being similar to the spherical neutrinosphere radius in the nonrotating model `nrot-HR`. The time- and angle-averaged ν_e and $\bar{\nu}_e$ luminosities of model `rot.6-MR` are similar to those of `nrot-HR` (Table 1). These differences are small enough that comparing these models allows us to roughly isolate the effects of rotation on the wind properties at a fixed epoch in the PNS cooling evolution (i.e., at approximately fixed neutrino luminosity).

Matter near the PNS surface in the rotational equator has high azimuthal velocity $v^{\phi} \gtrsim 0.2\,c$ due to the rapid rotation. Moving above the stellar surface, $v^{\phi} \propto 1/\varrho$, consistent with conservation of specific angular momentum in the wind, $\ell = \varrho v^{\phi} = {\rm const.}$ (Figure 5).

The isothermal surfaces are also oblate in shape, with a slightly higher neutrinosphere temperature (and hence mean neutrino energy) along the polar axis than in the equator (Figure 6). This difference may in part be attributable to the von Zeipel (1924) effect, whereby the effective temperature scales with the effective surface gravity $T_{\rm eff} \propto g_{\rm eff}^{1/4}$. Given that $g_{\rm eff}(R_{\rm eq})/g_{\rm eff}(R_{\rm p}) \sim [1 - \Omega^2/\Omega_{\rm K}^2] \sim 0.1$ for model `rot.6-MR`, this would predict $T_{\rm eff}(R_{\rm eq}) \lesssim 0.6T_{\rm p}(R_{\rm eq})$, close to the ratio of polar and equatorial mean neutrino energies (Figure 7).

The gain region around where $\dot{q}_{\rm net}$ peaks is also more radially extended in the equatorial region, but the peak heating rate $\dot{q}_{\rm net}$ is noticeably higher in the polar region, where it again resembles that seen in the nonrotating case. This enhancement of the polar heating rate results from the greater neutrino flux in this region and the higher mean neutrino energy (Figure 5). The neutrino heating rate drops off abruptly outside of the α-particle formation surface (see below), because the neutrino absorption cross section of α particles is much smaller than that of free nucleons.

The isotropic mass-loss rate $\dot{M} \sim 10^{-4}\,M_{\odot}\ {\rm s^{-1}}$ along the polar direction in model `rot.6-MR`, is similar to that of the nonrotating model `nrot-HR` (Figure 7). By contrast, the values of $\dot{M}$ in the equatorial plane are larger than those in the nonrotating case by one to two orders of magnitude, $\sim 10^{-3} - 10^{-2}\,M_{\odot}\ {\rm s^{-1}}$. Rotational enhancement of the mass-loss rate is a well known effect in thermally driven winds (e.g., Lamers & Cassinelli 1999, and references therein). Rotation has the effect of expanding the density scale height of the atmosphere $H \approx c_s^2/g_{\rm eff}$, where $g_{\rm eff} = g - a_c$, and g and a_c are the gravitational and centripetal acceleration experienced by material in the equator, respectively. A larger scale height exponentially increases the mass in the gain region (since $\rho \propto e^{-H/r}$), thus boosting $\dot{M}$ at the equator relative to the pole, despite the lower specific neutrino heating rate in the equatorial regions. Latitudinal mixing of the wind material occurs moving outwards with radius; however, an order of magnitude pole-to-equator difference in $\dot{M}$ is preserved to large radii $\gtrsim$120 km (Figure 7), outside the sonic surface where further mixing is unlikely to occur.

Another consequence of the lower specific heating rate in the equatorial plane is a suppression of the wind entropy with increasing polar angle. The entropy along the polar direction, $s \approx 70$, is similar to that of the nonrotating PNS wind solution, compared to $s \approx 20$ in the equatorial plane (Figure 7).

Since material in the rotational equator starts out more weakly bound to the star and receives less heating, the radial velocity v^r is lower there ($\lesssim 0.05\,c$) and matter is slower to become unbound. In the polar region, where the net neutrino heating is maximal, matter accelerates to supersonic velocities $v \approx 0.1\,c$ within a few hundred kilometers (Figure 5), significantly closer to the PNS than in the nonrotating case (Figure 2). This higher polar acceleration may result from "focusing" of the polar flow by the denser equatorial outflow (somewhat akin to the "de Laval nozzle" effect; Blandford & Rees 1974), which causes the areal function of the polar flow-lines to decrease with radius differently than the $\propto 1/r^2$ spherical outflow case.

Matter attains $E_{\rm tot} > 0$ and becomes unbound from the PNS along the polar directions by radii $z \approx 20$ km, while, in the equatorial regions, this is only achieved outside the α-formation surface at radii $\gtrsim$90 km (Figure 5). The significant heating due to α-particle formation ($\approx$7 MeV per nucleon) helps unbind still-marginally bound material, similar to as found in simulations of viscously spreading accretion disks in neutron star mergers (e.g., Fernández & Metzger 2013; Siegel & Metzger 2018). Given the low entropy of the outflow, just

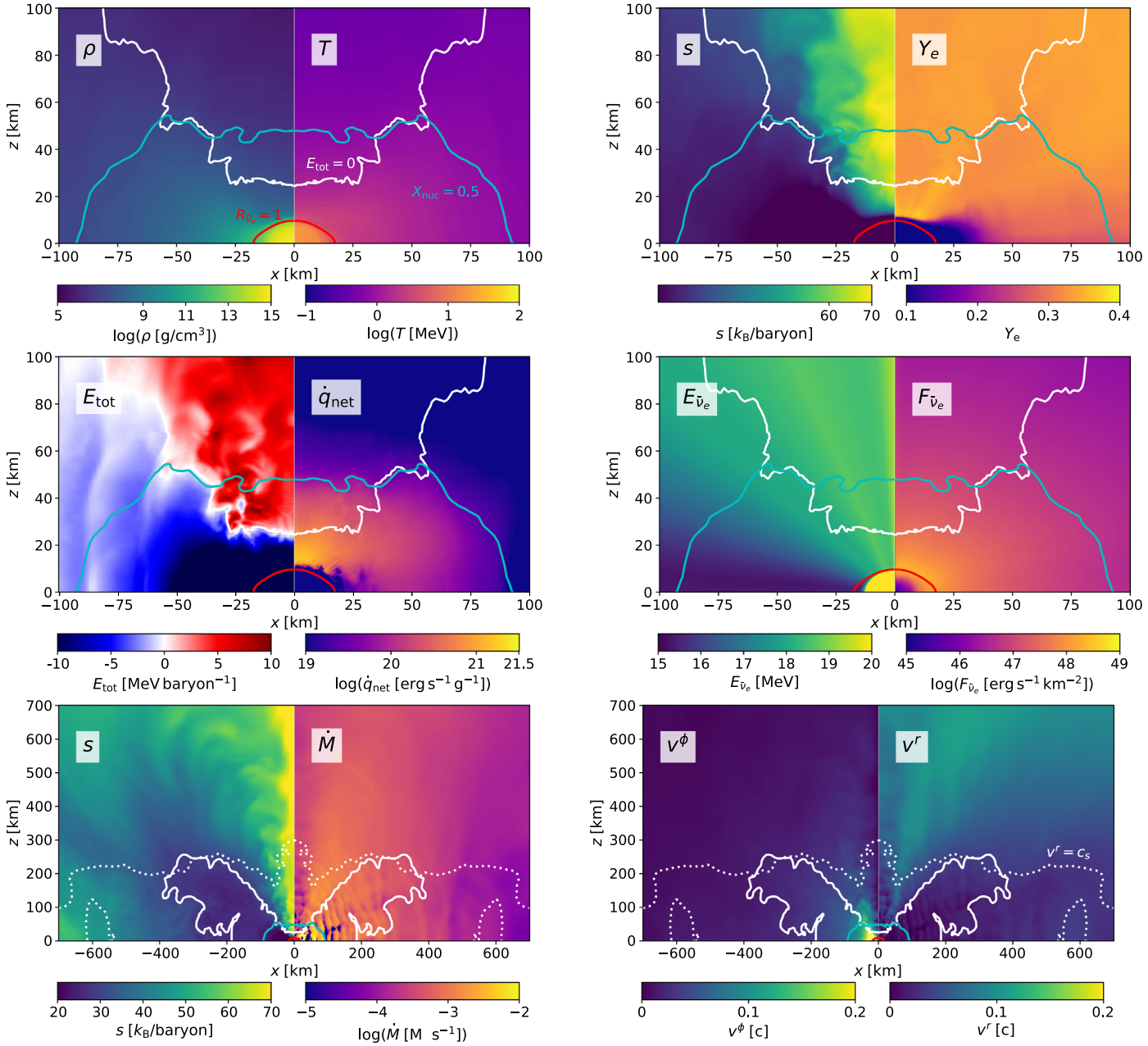

Figure 5. Similar to Figure 2, except now showing snapshots at $t = 100$ ms of two-dimensional slices through the rotational axis for model `rot.6-MR`, and including new quantities, such as azimuthal velocity v^ϕ, electron anti-neutrino flux $F_{\bar{\nu}_e}$, and mean energy $E_{\bar{\nu}_e}$. Please note the different radial scales in the top two rows compared to the bottom row.

outside this surface, the α particles rapidly assemble into seed nuclei, releasing further energy.

The asymptotic value of the wind electron fraction Y_e along the polar directions is $\approx$0.35, similar or moderately lower than that achieved in the nonrotating model (Figure 7). However, outflows from the equator regions are significantly more neutron rich, with $0.25 \lesssim Y_e \lesssim 0.3$. In both the polar and equatorial outflow regions, the wind composition still approaches equilibrium with the neutrino radiation field, as evidenced by $Y_e \approx Y_{e,\rm eq}^{\rm abs}$. The lower value of $Y_{e,\rm eq}^{\rm abs}$ (Equation (12)) and hence Y_e in the equatorial outflow results from the suppression of L_{ν_e} relative to $L_{\bar{\nu}_e}$ in this region, due to greater ν_e optical depth through the neutron-rich equatorial bulge. The large contrast between the temperatures at the ν_e and $\bar{\nu}_e$ neutrinospheres in the equatorial plane (Figure 6) gives rise to the distinct average neutrino energies of ν_e and $\bar{\nu}_e$ along these directions.

The strong angular dependence of several wind quantities also impacts the angular averaged wind properties as illustrated in Figure 8 (see also Table 2). Notably, the overall mass-loss rate is enhanced by one to two orders of magnitude for the most rapidly rotating model relative to the nonrotating model, while the overall entropy of the wind decreases to less than half of the value of the nonrotating model. As expected from the angular trends in Figure 7, Figure 8 also shows somewhat larger electron anti-neutrino luminosities, smaller electron anti-neutrino mean energies, and a smaller overall Y_e.

As a result of the strong angular dependence of $\{Y_e, v^r, s, T\}$ in the rotating models, the r-process figure of merit η also varies as a function of polar angle θ. Figure 9 compares the

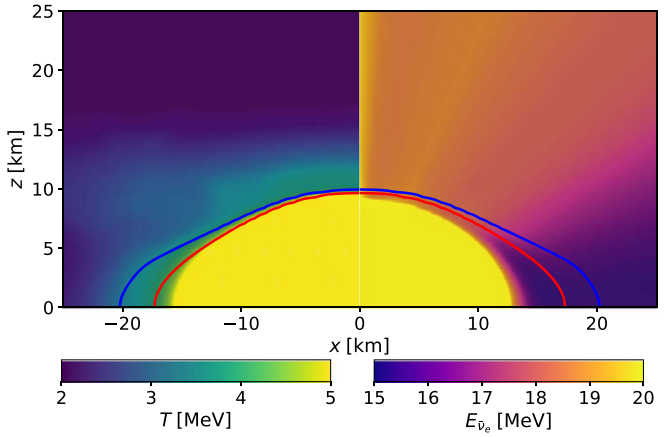

Figure 6. Temperature (left) and electron anti-neutrino mean energy (right) close to the PNS surface in the meridional plane for the maximally rotating model `rot.6-MR`. The approximate neutrinosphere surfaces (contours τ_{ν_e}, $\tau_{\bar{\nu}_e} = 1$) for ν_e and $\bar{\nu}_e$ are shown as blue and red curves, respectively. A bulge due to rapid rotation pushes out the location of the neutrinosphere near the equator, decreasing the $\tau = 1$ temperatures and reducing the mean neutrino energies in the equatorial regions relative to the polar regions.

angular profile of η from the rotating star simulations to the nonrotating model. In the polar region, the rotating and nonrotating models achieve a similar value $\eta \approx 3 - 6 \times 10^8$. However, in the equatorial region, η is significantly suppressed for the rotating models, with η being approximately two orders of magnitude lower for rot.7−MR and rot.6−MR. Taken together, the value of η lies well below the minimum threshold for second or third peak *r*-process element production for all outflow angles and all models. This disfavors rapidly spinning PNS as *r*-process sources via the α-rich freeze-out mechanism.

At face value, rotation appears to be detrimental to the *r* process in PNS winds. However, this does not account for the effect of a lower Y_e alone, absent an α-rich freeze-out. The value of Y_e in our most rapidly rotating models is ≈10% smaller in the equatorial direction than along the pole (we denote the Y_e-suppressed region with a dashed line in Figure 9) or in the nonrotating wind model with otherwise similar neutrino luminosities and energies. Thus, for example, if the "true" wind electron fraction at a given point in the cooling evolution of a nonrotating PNS were $Y_{e,0} \approx 0.45$–0.5, (e.g., Roberts et al. 2012; their Figure 5), rotation could act to reduce Y_e to $\approx 0.9 Y_{e,0} \approx 0.4 - 0.45$, sufficient to produce neutron-rich light element primary-process (LEPP) nuclei with $38 < Z < 47$ (e.g., Arcones & Montes 2011), even absent an α-rich freeze-out (i.e., even for arbitrarily low values of η).

4. Summary and Conclusions

We have explored the effects of rapid rotation on the properties of neutrino-heated PNS winds by means of three-dimensional GRHD simulations with M0 neutrino transport.

We calculate a suite of 1.4 $M_\odot$ PNS models corresponding to different solid-body rotation rates (Table 1), ranging from the nonrotating case studied in most previous works ($\Omega = 0$) to stars rotating near break-up ($\Omega/\Omega_K \simeq 0.94$; $P \simeq 1.11$ ms). We initialize the axisymmetric PNS structure using the RNS code integrated via a novel procedure with the SFHo tabulated EOS. Rather than following the self-consistent cooling evolution of the PNS from an initial post-explosion or post-merger state, we initialize the PNS temperature and Y_e radial profiles in β-equilibrium following Kaplan et al. (2014). The chosen temperature normalization generates steady-state neutrino

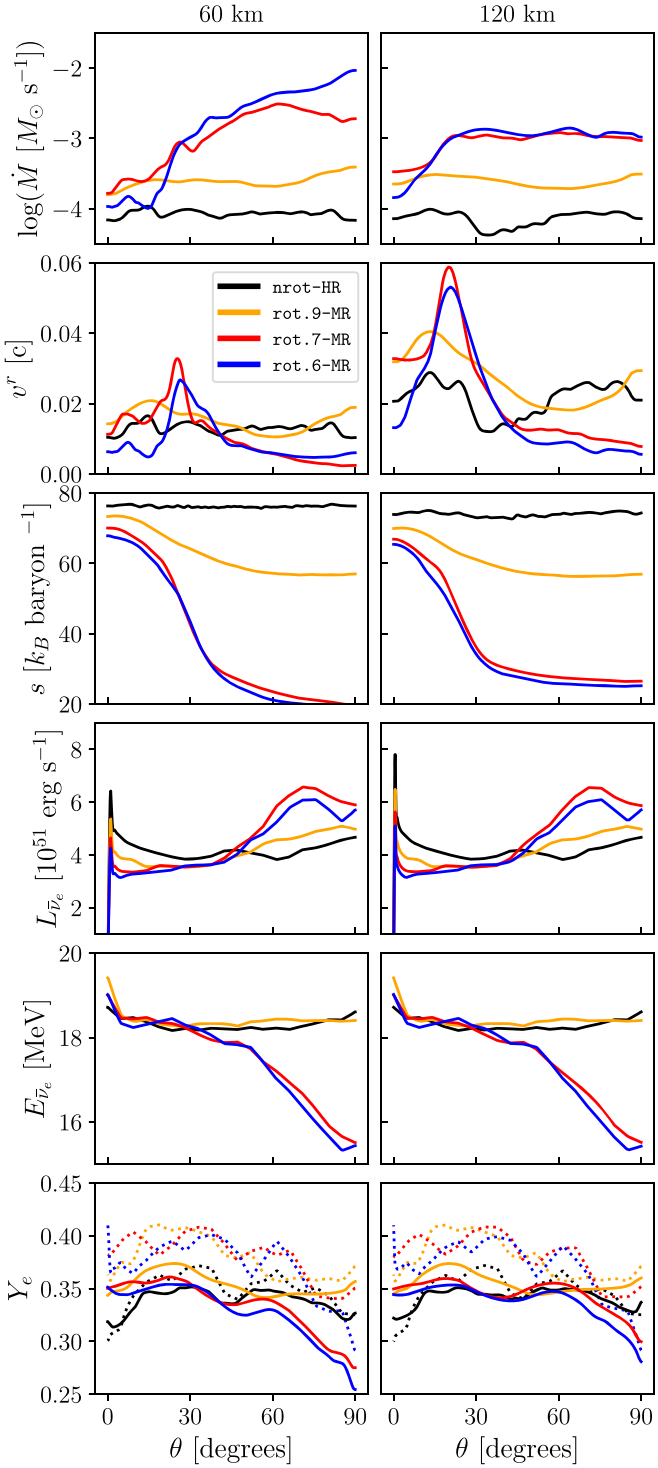

Figure 7. Wind properties as a function of polar angle θ, measured from the z-axis (rotation axis in rotating models), through spherical surfaces at $r = 60$ km (left) and $r = 120$ km (right) from the nonrotating model `nrot-HR` (nonrotating; black) and rotating models `rot.9-MR` (orange), `rot.7-MR` (red), and `rot.6-MR` (blue), time averaged over the final third of the simulation run (e.g., 100–150 ms for nrot−HR). From top to bottom, the quantities shown include isotropic mass-loss rate $\dot{M}$, radial velocity v^r, specific entropy s, isotropic electron anti-neutrino luminosity $L_{\bar{\nu}_e}$, mean electron anti-neutrino energy $E_{\bar{\nu}_e}$, and electron fraction Y_e. Dotted lines in the bottom panel show our estimate of the equilibrium electron fraction $Y_{e,\mathrm{eq}}^{\mathrm{abs}}$ (Equation (12)).

luminosities and energies close to those achieved on a timescale of seconds after a supernova explosion, and over which the bulk of the integrated wind mass loss will occur.

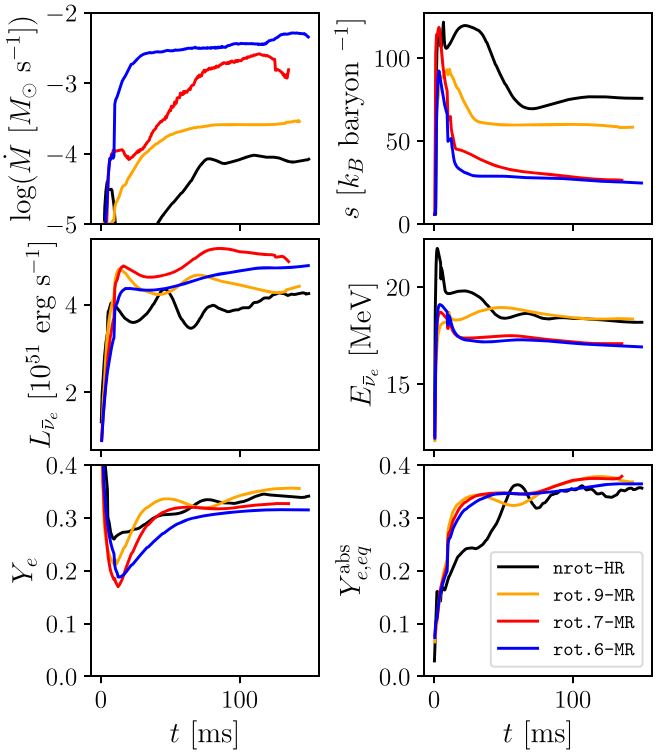

Figure 8. Similar to Figure 4, except now comparing angle-averaged wind properties in the nonrotating model `nrot-HR` (black), and rotating models `rot.9-MR` (orange), `rot.7-MR` (red), and `rot.6-MR` (blue) as measured through a spherical surface of radius $r = 60$ km.

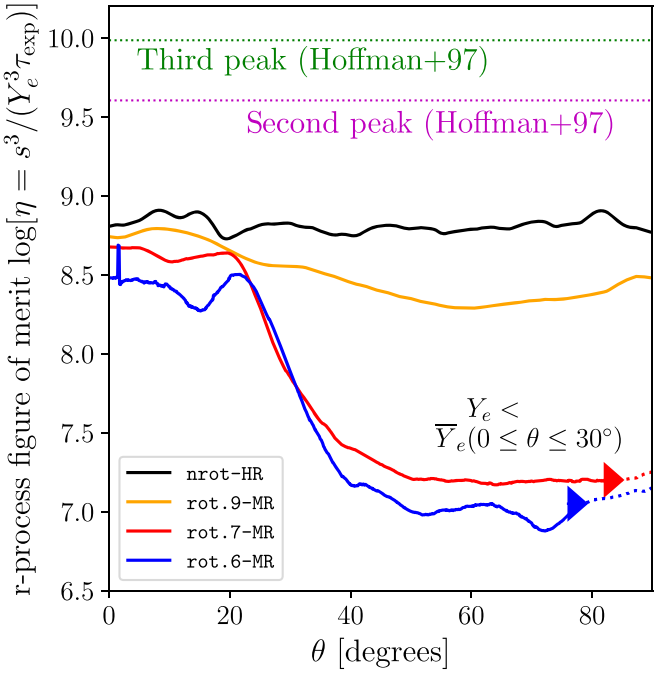

Figure 9. The r-process figure-of-merit parameter $\eta \equiv s_\infty^3/(Y_e^3 \tau_{\mathrm{exp}})$ (Equation (8)) as a function of outflow polar angle θ, where the relevant quantities are time-averaged and measured through the $T = 0.5$ MeV surface, shown separately for the models `nrot-HR`, `rot.9-MR`, `rot.7-MR`, and `rot.6-MR` as marked. For comparison we show the threshold value η_{thr} (Equation (8)) required for neutron captures to reach the second (purple dotted line) and third (green dotted line) r-process peaks (Hoffman et al. 1997). A dotted line to the right of the solid triangles in the rapidly rotating models (`rot.6-MR`, `rot.7-MR`) denotes the angles over which Y_e is 10% lower than its average value along the polar angles $0° < \theta < 30°$ (the latter is roughly similar to that obtained from a nonrotating wind for the same neutrino emission properties); the outflow from such regions may be capable of a successful r process even absent an α-rich freeze-out (i.e., even if $\eta \ll \eta_{\mathrm{thr}}$).

Our focus is on studying the wind properties in the gain layer above the PNS surface and out to large radii ($\sim$1000 km); however, we are not able to fully resolve the neutrinosphere decoupling region (Figure 1). As a consequence of this, as well as of our idealized initial temperature/Y_e structure, the partitioning between ν_e and $\bar{\nu}_e$ luminosities and their energies in our simulations do not match those predicted by supernova simulations, nor the resulting wind electron fractions $Y_e \simeq Y^{\mathrm{abs}}_{e,\mathrm{eq}}(L_{\nu_e,\bar{\nu}_e}, E_{\nu_e,\bar{\nu}_e})$. Specifically, our nonrotating wind solutions achieve values $Y_e \simeq 0.34$ (Figure 4) significantly lower than those found by detailed PNS cooling calculations, $Y_e \approx 0.45$–0.55 (e.g., Roberts & Reddy 2017; Pascal et al. 2022). Nevertheless, our simulations can still be used to explore the relative effects of rotation on Y_e through a comparison to otherwise equivalent nonrotating models with similar neutrino emission properties.

Our main conclusions can be summarized as follows.

1. After an initial transient phase, all of our models reach approximately steady outflow solutions with positive energies $E_{\mathrm{tot}} > 0$ and sonic surfaces captured on the computational grid, on timescales $\sim$100 ms (Figure 2, 3). We validate our nonrotating solutions by comparing them to time-independent spherical wind calculations (Table 3). Scaling our wind properties ($\dot{M}$, s_∞, τ_{exp}, v_∞) based on analytic expressions from Qian & Woosley (1996) given the relative neutrino properties (L_ν, E_ν, R_ν), we obtain good agreement (to within $\lesssim$10%) with Thompson et al. (2001).
2. Our nonrotating and slower rotating models (`rot.9-MR`; $\Omega/\Omega_{\mathrm{K}} \simeq 0.4$) exhibit approximately spherical outflow properties. In contrast, the fastest rotating models (`rot.7-MR`, `rot.6-MR`; $\Omega/\Omega_{\mathrm{K}} \gtrsim 0.75$) generate outflows with distinct properties near the equatorial plane versus higher latitudes closer to the rotational axis (Figure 5, Table 2). The outflow properties along the rotational axis ($\theta \lesssim 30°$) are qualitatively similar to those of the slowly rotating models in their key properties (e.g., $\dot{M}$, Y_e, s_∞, L_ν, E_ν; Figure 7), as would be expected because centrifugal effects are weak along these directions. However, outflows from intermediate latitudes accelerate faster to higher speeds compared to a spherical wind (Figure 7); these features may result from 'de Laval'-like focusing of polar streamlines by the denser equatorial outflow.
3. The equatorial outflows from rapidly rotating PNS exhibit qualitative differences from the nonrotating case (Figure 7), as expected because centrifugal forces have a large effect on the hydrostatic structure of the atmosphere for spin periods $P \ll P_{\mathrm{c}} \approx 3$ ms (Equation (13)). Relative to slowly rotating models, the equatorial outflows from rapid rotators possess: higher mass-loss rates $\dot{M}$ by over an order of magnitude in the fastest spinning case; slower acceleration and lower asymptotic radial velocities; and lower entropy s_∞ by a factor up to about four. These features may be understood as a consequence of the rotation-induced reduction in the effective gravitational mass, when applied to analytic predictions for the M dependence of the wind properties (Qian & Woosley 1996).

The equatorial outflows of the rapidly rotating solutions are also characterized by lower neutrino energies and a larger contrast between the ν_e and $\bar{\nu}_e$ neutrinospheres and their respective temperatures/luminosities; these features result from the presence of a dense neutron-rich equatorial bulge/decretion disk near the surface of the star (Figure 6). These changes in the $\nu_e/\bar{\nu}_e$ properties reduce the equilibrium electron fraction $Y_{e,\rm eq}^{\rm abs}$ (Equation (12); and hence $Y_e \lesssim 0.3$) of the equatorial outflows relative to the slowly rotating case.

4. Rapid rotation tends to reduce s_∞ and to increase $\tau_{\rm exp}$ as a result of the slower expansion speed in the dense equatorial outflow; both effects act to reduce the key parameter $\eta = s_\infty^3/(\tau_{\rm exp} Y_e^3)$ (Equation (8)) by over an order of magnitude in the rotating wind case (Figure 9). We conclude that rotation (at least absent a strong magnetic field) does not facilitate a successful second or third r process via the α-rich freeze-out mechanism.

   On the other hand, outflows near the equatorial plane in our fastest rotating models possess Y_e smaller by $\approx$10–15% compared to the otherwise equivalent non-rotating case. The winds from very rapidly spinning PNS could therefore generate nucleosynthetic abundance patterns that are quantitatively distinct from those of slowly rotating PNS, even neglecting potential rotation-induced changes to the PNS cooling evolution. For example, if slowly rotating PNS winds achieve $Y_e \gtrsim 0.5$–0.55 (e.g., Pascal et al. 2022) and generate mostly iron group elements and p-nuclei via the rp-process and νp-process (e.g., Fröhlich et al. 2006; Roberts et al. 2010; Fischer et al. 2010), rotating PNS winds could obtain $Y_e \lesssim 0.5$ and would instead synthesize neutron-rich LEPP or light r-process nuclei (e.g., Qian & Wasserburg 2007; Arcones & Montes 2011).
5. The neutrino luminosities achieved by our models of a few $\times\, 10^{51}$ erg s^{-1} will last for a timescale $\tau_{\rm c} \approx 3$ seconds after a successful supernova explosion (Roberts & Reddy 2017; their Figure 3). Although our simulations are not run this long, our most rapidly spinning PNS solutions therefore predict a total wind-ejecta mass $\sim \dot{M}\tau_{\rm c} \approx 3 \times 10^{-3}\ M_\odot$ comprised of more neutron-rich nuclei than would accompany the birth of a slowly rotating PNS of otherwise similar properties (which produce only $\approx 10^{-4}\ M_\odot$ in total wind ejecta; e.g., Thompson et al. 2001).

   Several strains of observational (e.g., Faucher-Giguère & Kaspi 2006; Vink & Kuiper 2006; Perna et al. 2008) and theoretical (e.g., Ma & Fuller 2019) evidence indicate that the birth of neutron stars with rapid spin periods $P \approx 1$ ms are rare in nature among the core-collapse population. However, given their larger wind-ejecta mass yields (by a factor $\gtrsim$10), even if such rapidly spinning PNS are formed in only $\sim$10% of all core-collapse supernovae, their total nucleosynthetic contribution may be competitive with "ordinary" supernovae birthing slowly spinning PNS. Broad-lined supernovae with atypically large ejecta kinetic energies (hinting at an important role of rotation in facilitating the explosion) indeed represent $\sim$10% of core-collapse explosions (e.g., Perley et al. 2020). The contributions of rapidly spinning PNS on individual "pollution events" observed in the surface abundances of halo stars (e.g., Honda et al. 2006; Spite et al. 2018) will be further enhanced if stellar cores retain greater angular momentum at core collapse at lower metallicity (e.g., Yoon & Langer 2005).

   Hot, rapidly spinning PNS-like stars are also generated from the merger of binary neutron stars (e.g., Dessart et al. 2009), albeit with higher masses $\gtrsim 2\,M_\odot$ than assumed in our models. However, the limited lifetimes of most such objects before they lose rotational support and collapse into a black hole may limit the contribution of their neutrino-driven winds relative to other sources of mass ejection during the merger and its aftermath (though strong magnetic fields may change this picture; e.g., Siegel et al. 2014; Metzger et al. 2018; Curtis et al. 2021).

Our present setup incorporates neutrino transport using an M0 scheme, which neglects the effects of lateral transport. This is likely a good approximation in our case because deviations from spherical symmetry are fairly modest and (compared, e.g., to simulations of the supernova explosion; Skinner et al. 2016) we are mainly interested in the properties of the outflows above the neutrino decoupling region. However, future work should aim to explore the impact of more accurate neutrino transport in the rapidly rotating cases.

In this paper, we have focused on an idealized numerical experiment to explore the effects of rotation on PNS winds in a controlled and general way. However, with the results now benchmarked, we can explore more realistic (albeit specific) PNS configurations from core-collapse SNe or NS mergers with the same code infrastructure. In the context of a self-consistent core-collapse SN or NS merger, the specifics of the neutrino luminosities and energies, Y_e profile near the PNS surface, and the large-scale environment, will differ from those we have assumed. As an example of the latter, in an NS merger, the PNS will be surrounded by an accretion torus, which generates its own outflow that may interact with the PNS wind (e.g., Metzger & Fernández 2014; Perego et al. 2014); likewise, at early times after an SN explosion, the PNS wind may catch up to the SN shock (e.g., Arcones et al. 2007). Although quantitative features of the wind, particularly the asymptotic Y_e values, may differ substantially due to these effects, the qualitative features (and the quantitative results for other properties set near the PNS surface such as $\dot{M}$ and the outflow entropy) are likely to be robust.

The study presented here also lays the groundwork for future three-dimensional simulation work including additional physical effects. One of the most important are those arising from a strong, ordered magnetic field, which may accompany the birth of rapidly spinning PNS as a result of dynamo processes which tap into the energy available in rotation or convection (e.g., Thompson & Duncan 1993; Siegel et al. 2013; Mösta et al. 2014; Raynaud et al. 2020). Magnetic fields of strength $\gtrsim 10^{14} - 10^{15}$ G comparable to those of Galactic magnetars have been shown to have major effects on the PNS wind properties and their efficacy in generating r-process elements, both with (e.g., Thompson et al. 2004; Metzger et al. 2007; Winteler et al. 2012; Vlasov et al. 2014, 2017) and without (e.g., Thompson 2003; Thompson & ud-Doula 2018) rapid rotation.

We thank Erik Schnetter, Ben Margalit, and Luciano Combi for discussions and support. This research was enabled in part by support provided by SciNet (www.scinethpc.ca) and Compute Canada (www.computecanada.ca). D.D. and

B.D.M. acknowledge support from the National Science Foundation (grant #AST-2002577). D.M.S. acknowledges the support of the Natural Sciences and Engineering Research Council of Canada (NSERC), funding reference number RGPIN-2019-04684. Research at Perimeter Institute is supported in part by the Government of Canada through the Department of Innovation, Science and Economic Development Canada and by the Province of Ontario through the Ministry of Colleges and Universities.

Software: The Einstein Toolkit (Löffler et al. 2012; http://einsteintoolkit.org), GRMHD con2prim (Siegel & Mösta 2018), PyCactus (Kastaun 2021), Matplotlib (Hunter 2007), NumPy (Harris et al. 2020), SciPy (Virtanen et al. 2020), and hdf5 (The HDF Group 1997–2022).

ORCID iDs

Dhruv Desai https://orcid.org/0000-0002-8914-4259
Daniel M. Siegel https://orcid.org/0000-0001-6374-6465
Brian D. Metzger https://orcid.org/0000-0002-4670-7509

References

Arcones, A., & Janka, H. T. 2011, A&A, 526, A160
Arcones, A., Janka, H. T., & Scheck, L. 2007, A&A, 467, 1227
Arcones, A., Janka, H.-T., & Scheck, L. 2007, A&A, 467, 1227
Arcones, A., & Montes, F. 2011, ApJ, 731, 5
Babiuc-Hamilton, M., Brandt, S. R., Diener, P., et al. 2019, The Einstein Toolkit , Zenodo, doi:10.5281/zenodo.3522086
Beloborodov, A. M. 2003, ApJ, 588, 931
Beloborodov, A. M. 2010, MNRAS, 407, 1033
Bhattacharya, M., Horiuchi, S., & Murase, K. 2021, arXiv:2111.05863
Blandford, R. D., & Rees, M. J. 1974, MNRAS, 169, 395
Bruenn, S. W. 1985, ApJS, 58, 771
Bucciantini, N., Quataert, E., Arons, J., Metzger, B. D., & Thompson, T. A. 2007, MNRAS, 380, 1541
Burrows, A., & Lattimer, J. M. 1986, ApJ, 307, 178
Burrows, A., Radice, D., Vartanyan, D., et al. 2020, MNRAS, 491, 2715
Cardall, C. Y., & Fuller, G. M. 1997, ApJL, 486, L111
Colella, P., & Woodward, P. R. 1984, JCoPh, 54, 174
Curtis, S., Mösta, P., Wu, Z., et al. 2021, arXiv:2112.00772
Dessart, L., Ott, C. D., Burrows, A., Rosswog, S., & Livne, E. 2009, ApJ, 690, 1681
Duan, H., & Qian, Y. 2004, Phs. Rev. D, 69, 123004
Duncan, R. C., Shapiro, S. L., & Wasserman, I. 1986, ApJ, 309, 141
Faucher-Giguère, C.-A., & Kaspi, V. M. 2006, ApJ, 643, 332
Fernández, R., & Metzger, B. D. 2013, MNRAS, 435, 502
Fischer, T., Martínez-Pinedo, G., Hempel, M., & Liebendörfer, M. 2012, PhRvD, 85, 083003
Fischer, T., Whitehouse, S. C., Mezzacappa, A., Thielemann, F.-K., & Liebendörfer, M. 2010, A&A, 517, A80
Freiburghaus, C., Rosswog, S., & Thielemann, F.-K. 1999, ApJ, 525, L121
Fröhlich, C., Hauser, P., Liebendörfer, M., et al. 2006, ApJ, 637, 415
Galeazzi, F., Kastaun, W., Rezzolla, L., & Font, J. A. 2013, PhRvD, 88, 064009
Goodale, T., Allen, G., Lanfermann, G., et al. 2003, in Vector and Parallel Processing—VECPAR'2002, 5th Int. Conf., Lecture Notes in Computer Science (Springer: Berlin)
Gossan, S. E., Fuller, J., & Roberts, L. F. 2020, MNRAS, 491, 5376
Harris, C. R., Millman, K. J., van der Walt, S. J., et al. 2020, Natur, 585, 357
Harten, A., Lax, P. D., & van Leer, B. 1983, SIAMR, 25, 35
Hempel, M., & Schaffner-Bielich, J. 2010, NuPhA, 837, 210
Hoffman, R. D., Woosley, S. E., & Qian, Y.-Z. 1997, ApJ, 482, 951
Honda, S., Aoki, W., Ishimaru, Y., Wanajo, S., & Ryan, S. G. 2006, ApJ, 643, 1180
Hüdepohl, L., Müller, B., Janka, H.-T., Marek, A., & Raffelt, G. G. 2010, PhRvL, 104, 251101
Hunter, J. D. 2007, CSE, 9, 90
Kajino, T., Otsuki, K., Wanajo, S., Orito, M., & Mathews, G. J. 2000, in Proc. of the First Asian-Pacific Conf., Few-Body Problems in Physics '99, ed. S. Oryu, S. Kamimura, & M. Ishikawa (New York: Springer)
Kaplan, J. D., Ott, C. D., O'Connor, E. P., et al. 2014, ApJ, 790, 19
Kastaun, W. 2021, PyCactus: Post-processing tools for Cactus computational toolkit simulation data, Astrophysics Source Code Library, ascl:2107.017
Lamers, H. J. G. L. M., & Cassinelli, J. P. 1999, in Introduction to Stellar Winds, ed. H. J. G. L. M. Lamers & J. P. Cassinelli (Cambridge: Cambridge Univ. Press)
Lippuner, J., & Roberts, L. F. 2015, ApJ, 815, 82
Löffler, F., Faber, J., Bentivegna, E., et al. 2012, CQGra, 29, 115001
Ma, L., & Fuller, J. 2019, MNRAS, 488, 4338
Martínez-Pinedo, G., Fischer, T., Lohs, A., & Huther, L. 2012, PhRvL, 109, 251104
Metzger, B. D., & Fernández, R. 2014, MNRAS, 441, 3444
Metzger, B. D., Giannios, D., & Horiuchi, S. 2011a, MNRAS, 415, 2495
Metzger, B. D., Giannios, D., Thompson, T. A., Bucciantini, N., & Quataert, E. 2011b, MNRAS, 413, 2031
Metzger, B. D., Thompson, T. A., & Quataert, E. 2007, ApJ, 659, 561
Metzger, B. D., Thompson, T. A., & Quataert, E. 2008, ApJ, 676, 1130
Metzger, B. D., Thompson, T. A., & Quataert, E. 2018, ApJ, 856, 101
Meyer, B. S. 2002, PhRvL, 89, 231101
Meyer, B. S., & Brown, J. S. 1997, ApJS, 112, 199
Meyer, B. S., Mathews, G. J., Howard, W. M., Woosley, S. E., & Hoffman, R. D. 1992, ApJ, 399, 656
Mösta, P., Richers, S., Ott, C. D., et al. 2014, ApJL, 785, L29
Nakazato, K., Sumiyoshi, K., Suzuki, H., et al. 2013, ApJS, 205, 2
Neilsen, D., Liebling, S. L., Anderson, M., et al. 2014, PhRvD, 89, 104029
Otsuki, K., Tagoshi, H., Kajino, T., & Wanajo, S.-y. 2000, ApJ, 533, 424
Pascal, A., Novak, J., & Oertel, M. 2022, MNRAS, 511, 356
Perego, A., Rosswog, S., Cabezón, R. M., et al. 2014, MNRAS, 443, 3134
Perley, D. A., Fremling, C., Sollerman, J., Miller, A. A., et al. 2020, ApJ, 904, 35
Perna, R., Soria, R., Pooley, D., & Stella, L. 2008, MNRAS, 384, 1638
Pons, J. A., Reddy, S., Prakash, M., Lattimer, J. M., & Miralles, J. A. 1999, ApJ, 513, 780
Qian, Y., & Woosley, S. E. 1996, ApJ, 471, 331
Qian, Y.-Z., Fuller, G. M., Mathews, G. J., et al. 1993, PhRvL, 71, 1965
Qian, Y.-Z., & Wasserburg, G. J. 2007, PhR, 442, 237
Qian, Y.-Z., & Woosley, S. E. 1996, ApJ, 471, 331
Radice, D., Galeazzi, F., Lippuner, J., et al. 2016, MNRAS, 460, 3255
Radice, D., Perego, A., Hotokezaka, K., et al. 2018, ApJ, 869, 130
Raynaud, R., Guilet, J., Janka, H.-T., & Gastine, T. 2020, SciA, 6, eaay2732
Roberts, L. F. 2012, ApJ, 755, 126
Roberts, L. F., & Reddy, S. 2017, in Handbook of Supernovae, ed. A. W. Alsabti & P. Murdin (New York: Springer International Publishing), 1605
Roberts, L. F., Reddy, S., & Shen, G. 2012, PhRvC, 86, 065803
Roberts, L. F., Shen, G., Cirigliano, V., et al. 2012, PhRvL, 108, 061103
Roberts, L. F., Woosley, S. E., & Hoffman, R. D. 2010, ApJ, 722, 954
Ruffert, M., Janka, H.-T., & Schaefer, G. 1996, A&A, 311, 532
Scheck, L., Kifonidis, K., Janka, H.-T., & Müller, E. 2006, A&A, 457, 963
Schnetter, E., Hawley, S. H., & Hawke, I. 2004, CQG, 21, 1465
Siegel, D. M., Ciolfi, R., Harte, A. I., & Rezzolla, L. 2013, PhRvD, 87, 121302
Siegel, D. M., Ciolfi, R., & Rezzolla, L. 2014, ApJL, 785, L6
Siegel, D. M., & Metzger, B. D. 2017, PhRvL, 119, 231102
Siegel, D. M., & Metzger, B. D. 2018, ApJ, 858, 52
Siegel, D. M., & Mösta, P. 2018, GRMHD_con2prim: a framework for the recovery of primitive variables in general-relativistic magnetohydrodynamics, Zenodo, doi:10.5281/zenodo.1213306
Siegel, D. M., Mösta, P., Desai, D., & Wu, S. 2018, ApJ, 859, 71
Skinner, M. A., Burrows, A., & Dolence, J. C. 2016, ApJ, 831, 81
Spite, F., Spite, M., Barbuy, B., et al. 2018, A&A, 611, A30
Steiner, A. W., Hempel, M., & Fischer, T. 2013, ApJ, 774, 17
Stergioulas, N., & Friedman, J. L. 1995, ApJ, 444, 306
Sumiyoshi, K., Suzuki, H., Otsuki, K., Terasawa, M., & Yamada, S. 2000, PASJ, 52, 601
Suzuki, T. K., & Nagataki, S. 2005, ApJ, 628, 914
Takahashi, K., Witti, J., & Janka, H.-T. 1994, A&A, 286, 857
The HDF Group, Witti, J., & Janka, H.-T. 1997–2022, Hierarchical data format, v5, http://www.hdfgroup.org/HDF5
Thompson, C., & Duncan, R. C. 1993, ApJ, 408, 194
Thompson, T. A. 2003, ApJL, 585, L33
Thompson, T. A., Burrows, A., & Meyer, B. S. 2001, ApJ, 562, 887
Thompson, T. A., Chang, P., & Quataert, E. 2004, ApJ, 611, 380

Thompson, T. A., & ud-Doula, A. 2018, MNRAS, 476, 5502
Thornburg, J. 2004, CQG, 21, 3665
Tóth, G. 2000, JCPH, 161, 605
Vink, J., & Kuiper, L. 2006, MNRAS, 370, L14
Virtanen, P., Gommers, R., Oliphant, T. E., et al. 2020, Nature Methods, 17, 261
Vlasov, A. D., Metzger, B. D., Lippuner, J., Roberts, L. F., & Thompson, T. A. 2017, MNRAS, 468, 1522
Vlasov, A. D., Metzger, B. D., & Thompson, T. A. 2014, MNRAS, 444, 3537
von Zeipel, H. 1924, MNRAS, 84, 665
Wanajo, S. 2013, ApJL, 770, L22
Winteler, C., Käppeli, R., Perego, A., et al. 2012, ApJL, 750, L22
Woosley, S. E., & Hoffman, R. D. 1992, ApJ, 395, 202
Woosley, S. E., Wilson, J. R., Mathews, G. J., Hoffman, R. D., & Meyer, B. S. 1994, ApJ, 433, 229
Yoon, S.-C., & Langer, N. 2005, A&A, 435, 967